Chapter 4

Feature detection and matching

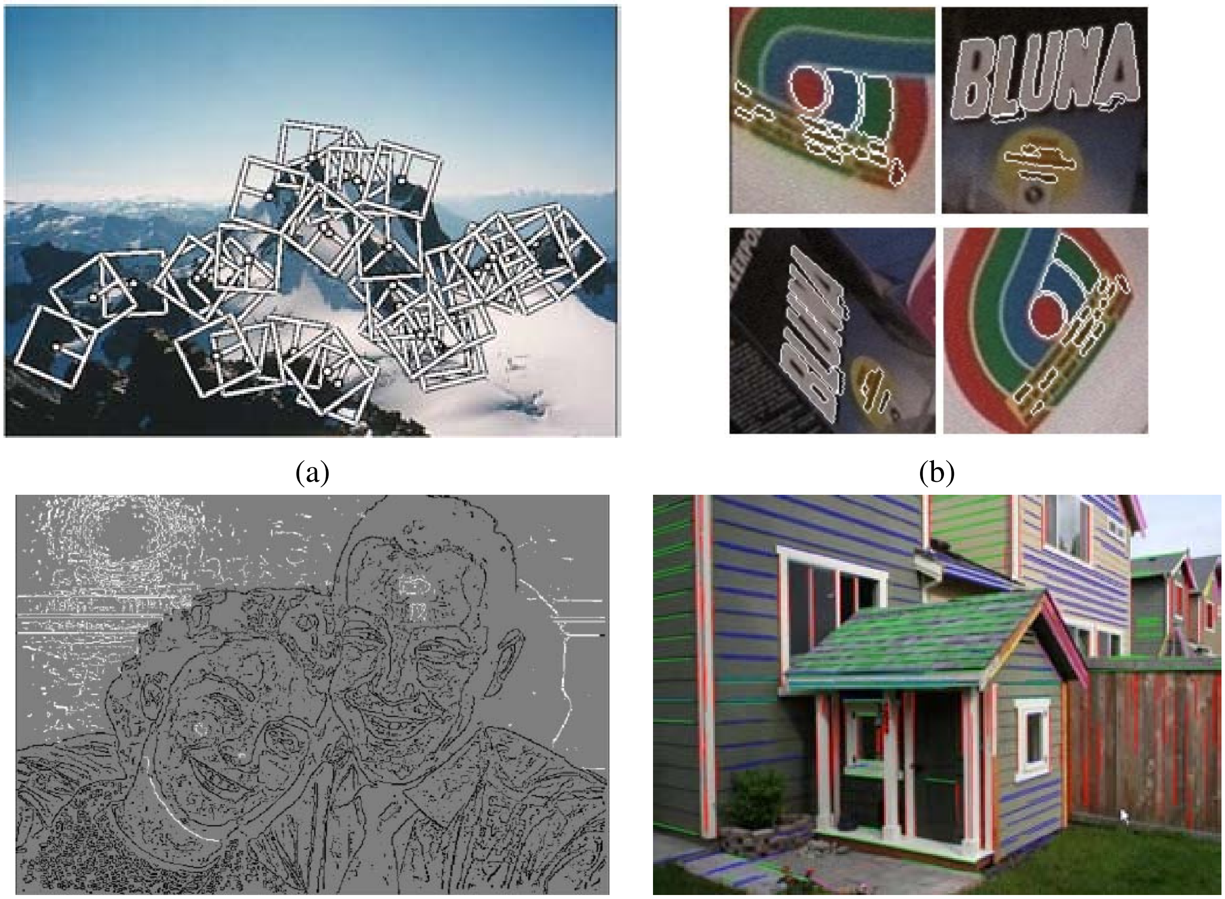

(a) (b)

(c) (d)

Figure 4.1: *A variety of feature detector and descriptors can be used to analyze describe and match images: (a) point-like interest operators (Brown* et al. *2005); (b) region-like interest operators (Brown* et al. *2005); (c) edges (Elder and Golderg 2001); (d) straight lines (Sinha* et al. *2008).*

Feature detection and matching are an essential component of many computer vision applications. Consider the two pairs of images shown in Figure 4.2. For the first pair, we may wish to *align* the two images so that they can be seamlessly stitched into a composite mosaic §9. For the second pair, we may wish to establish a dense set of *correspondences* so that a 3D model can be constructed or an in-between view could be generated §11. In either case, what kinds of *features* should you detect and then match in order to establish such an alignment or set of correspondences? Think about this for a few moments before reading on.

The first kind of feature that you may notice are specific locations in the images, such as mountain peaks, building corners, doorways, or interestingly shaped patches of snow. These kinds of localized features are often called *keypoint features* or *interest points* (or even *corners*) and are often described by the appearance of *patches* of pixels surrounding the point location §4.1. Another class of important features are *edges*, e.g., the profile of the mountains against the sky §4.2. These kinds of features can be matched based on their orientation and local appearance (*edge profiles*) and can also be good indicators of object boundaries and *occlusion* events in image sequences. Edges can be grouped into longer *curves* and *straight line segments*, which can be directly matched, or analyzed to find *vanishing points* and hence internal and external camera parameters §4.3.

In this chapter, we describe some practical approaches to detecting such features and also discuss how feature correspondences can be established across different images. Point features are now used in such a wide variety of applications that I encourage everyone to read and implement some of the algorithms from §4.1. Edges and lines provide information that is complementary to both keypoint and region-based descriptors and are well-suited to describing object boundaries and man-made objects. These alternative descriptors, while extremely useful, can be skipped in a short introductory course.

4.1 Points

Point features can be used to find a sparse set of corresponding locations in different images, often as a pre-cursor to computing camera pose §7, which is a prerequisite for computing a denser set of correspondences using stereo matching §11. Such correspondences can also be used to align different images, e.g., when stitching image mosaics or performing video stabilization §9. They are also used extensively to perform object instance and category recognition §14.3-§14.4. A key advantage of keypoints is that they permit matching even in the presence of clutter (occlusion) and large scale and orientation changes.

Feature-based correspondence techniques have been used since the early days of stereo matching (Hannah 1974, Moravec 1983, Hannah 1988) and have more recently gained popularity for image stitching applications (Zoghlami *et al.* 1997, Capel and Zisserman 1998, Cham and Cipolla

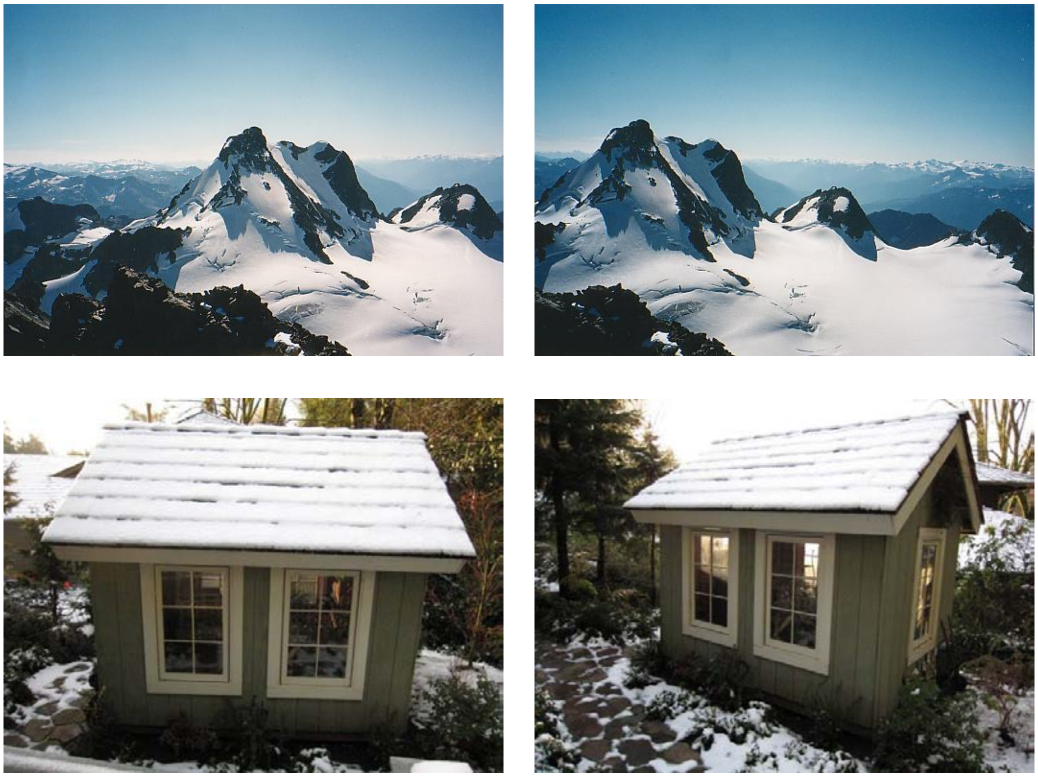

Figure 4.2: *Two pairs of images to be matched. What kinds of features might one use to establish a set of* correspondences *between these images?*

1998, Badra *et al.* 1998, McLauchlan and Jaenicke 2002, Brown and Lowe 2007, Brown *et al.* 2005) as well as fully automated 3D modeling (Beardsley *et al.* 1996, Schaffalitzky and Zisserman 2002, Brown and Lowe 2003, Snavely *et al.* 2006). *[Note: Thin out some of these references?]*

There are two main approaches to finding feature points and their correspondences. The first is to find features in one image that can be accurately *tracked* using a local search technique such as correlation or least squares §4.1.4. The second is to independently detect features in all the images under consideration and then *match* features based on their local appearance §4.1.3. The former approach is more suitable when images are taken from nearby viewpoints or in rapid succession (e.g., video sequences), while the latter is more suitable when a large amount of motion or appearance change is expected, e.g., in stitching together panoramas (Brown and Lowe 2007), establishing correspondences in *wide baseline stereo* (Schaffalitzky and Zisserman 2002), or performing object recognition (Fergus *et al.* 2003).

In this section, we split the keypoint detection and matching pipeline into four separate stages. During the first *feature detection* (extraction) stage, §4.1.1, each image is searched for locations that are likely to match well in other images. At the second *feature description* stage, §4.1.2, each

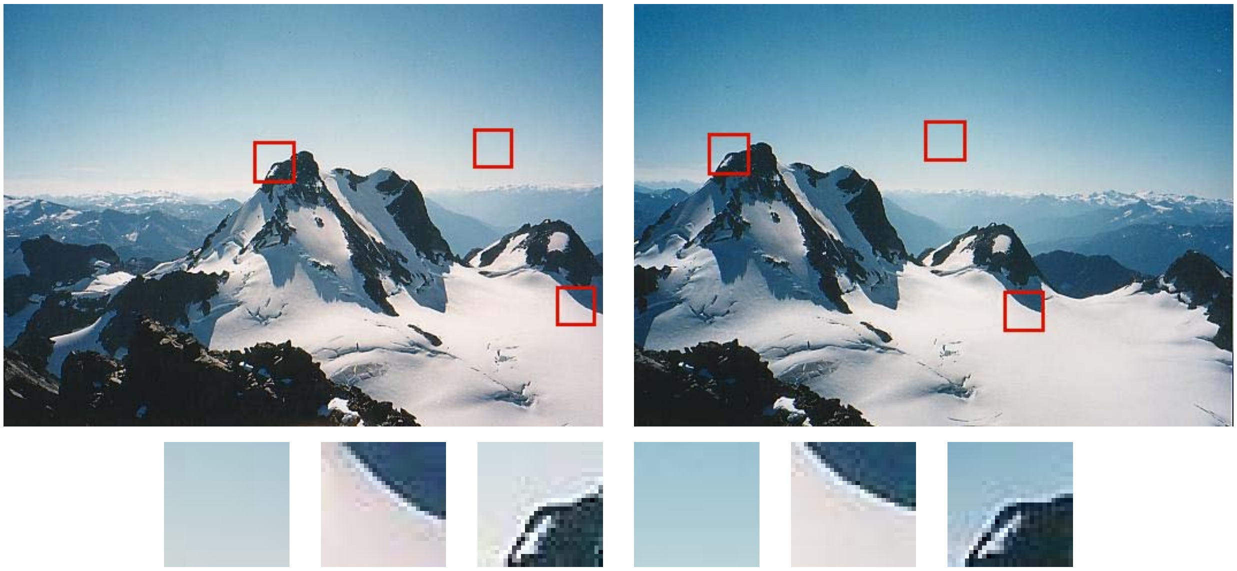

Figure 4.3: *Image pairs with extracted patches below. Notice how some patches can be localized or matched with higher accuracy than others.*

region around detected keypoint locations in converted into a more compact and stable (invariant) *descriptor* that can be matched against other descriptors. The third *feature matching* stage, §4.1.3, efficiently searches for likely matching candidates in other images. The fourth *feature tracking* stage, §4.1.4, is an alternative to the third stage that only searches a small neighborhood around each detected feature and is therefore more suitable for video processing.

A wonderful example of all of these stages can be found in David Lowe's (2004) *Distinctive image features from scale-invariant keypoints* paper, which describes the development and refinement of his *Scale Invariant Feature Transform* (SIFT). Comprehensive descriptions of alternative techniques can be found in a series of survey and evaluation papers by Schmid, Mikolajczyk, *et al.* covering both feature detection (Schmid *et al.* 2000, Mikolajczyk *et al.* 2005, Tuytelaars and Mikolajczyk 2007) and feature descriptors (Mikolajczyk and Schmid 2005). Shi and Tomasi (1994) and Triggs (2004) also provide nice reviews of feature detection techniques.

4.1.1 Feature detectors

How can we find image locations where we can reliably find correspondences with other images, i.e., what are *good features to track* (Shi and Tomasi 1994, Triggs 2004)? Look again at the image pair shown in Figure 4.3 and at the three sample *patches* to see how well they might be matched or tracked. As you may notice, textureless patches are nearly impossible to localize. Patches with large contrast changes (gradients) are easier to localize, although straight line segments at a single

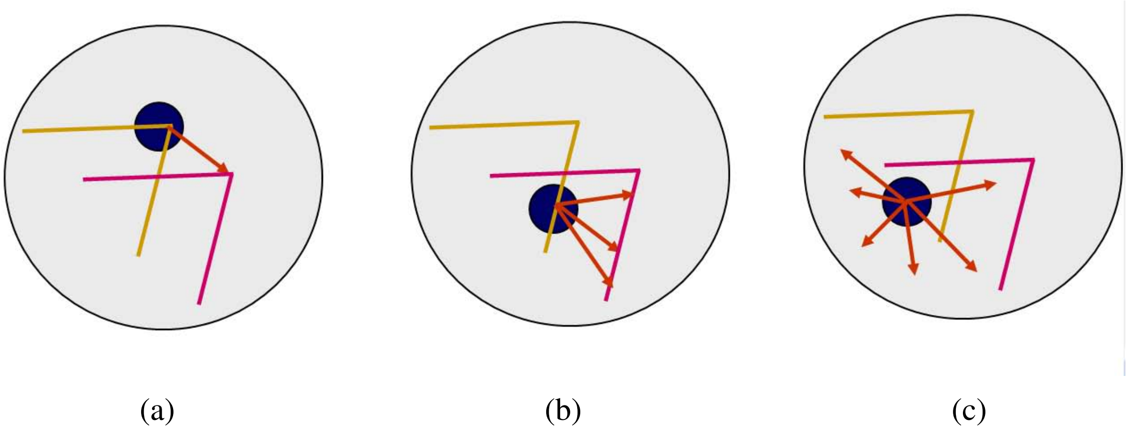

Figure 4.4: *Aperture problems for different image patches: (a) stable ("corner-like") flow; (b) classic aperture problem (barber-pole illusion); (c) textureless region. The two images I_0 (yellow) and I_1 (red) are overlaid. The red vector $\boldsymbol{u}$ indicates the displacement between the patch centers, and the $w(\boldsymbol{x}_i)$ weighting function (patch window) is shown as a dark circle.*

orientation suffer from the *aperture problem* (Horn and Schunck 1981, Lucas and Kanade 1981, Anandan 1989), i.e., it is only possible to align the patches along the direction *normal* to the edge direction (Figure 4.4b). Patches with gradients in at least two (significantly) different orientations are the easiest to localize, as shown schematically in Figure 4.4a.

These intuitions can be formalized by looking at the simplest possible matching criterion for comparing two image patches, i.e., their (weighted) summed square difference,

$$E_{\text{WSSD}}(\boldsymbol{u}) = \sum_i w(\boldsymbol{x}_i)[I_1(\boldsymbol{x}_i + \boldsymbol{u}) - I_0(\boldsymbol{x}_i)]^2, \tag{4.1}$$

where I_0 and I_1 are the two images being compared, $\boldsymbol{u} = (u, v)$ is the *displacement* vector, and $w(\boldsymbol{x})$ is a spatially varying weighting (or window) function. (Note that this is the same formulation we later use to estimate motion between complete *images* §8.1, and that this section shares some material with that later section.)

When performing feature detection, we do not know which other image location(s) the feature will end up being matched against. Therefore, we can only compute how stable this metric is with respect to small variations in position $\Delta\boldsymbol{u}$ by comparing an image patch against itself, which is known as an *auto-correlation function* or *surface*

$$E_{\text{AC}}(\Delta\boldsymbol{u}) = \sum_i w(\boldsymbol{x}_i)[I_0(\boldsymbol{x}_i + \Delta\boldsymbol{u}) - I_0(\boldsymbol{x}_i)]^2 \tag{4.2}$$

(Figure 4.5).[1] Note how the auto-correlation surface for the textured flower bed (Figure 4.5b, red

[1] Strictly speaking, the auto-correlation is the *product* of the two weighted patches; I'm using the term here in a more qualitative sense. The weighted sum of squared differences is often called an *SSD surface* §8.1.

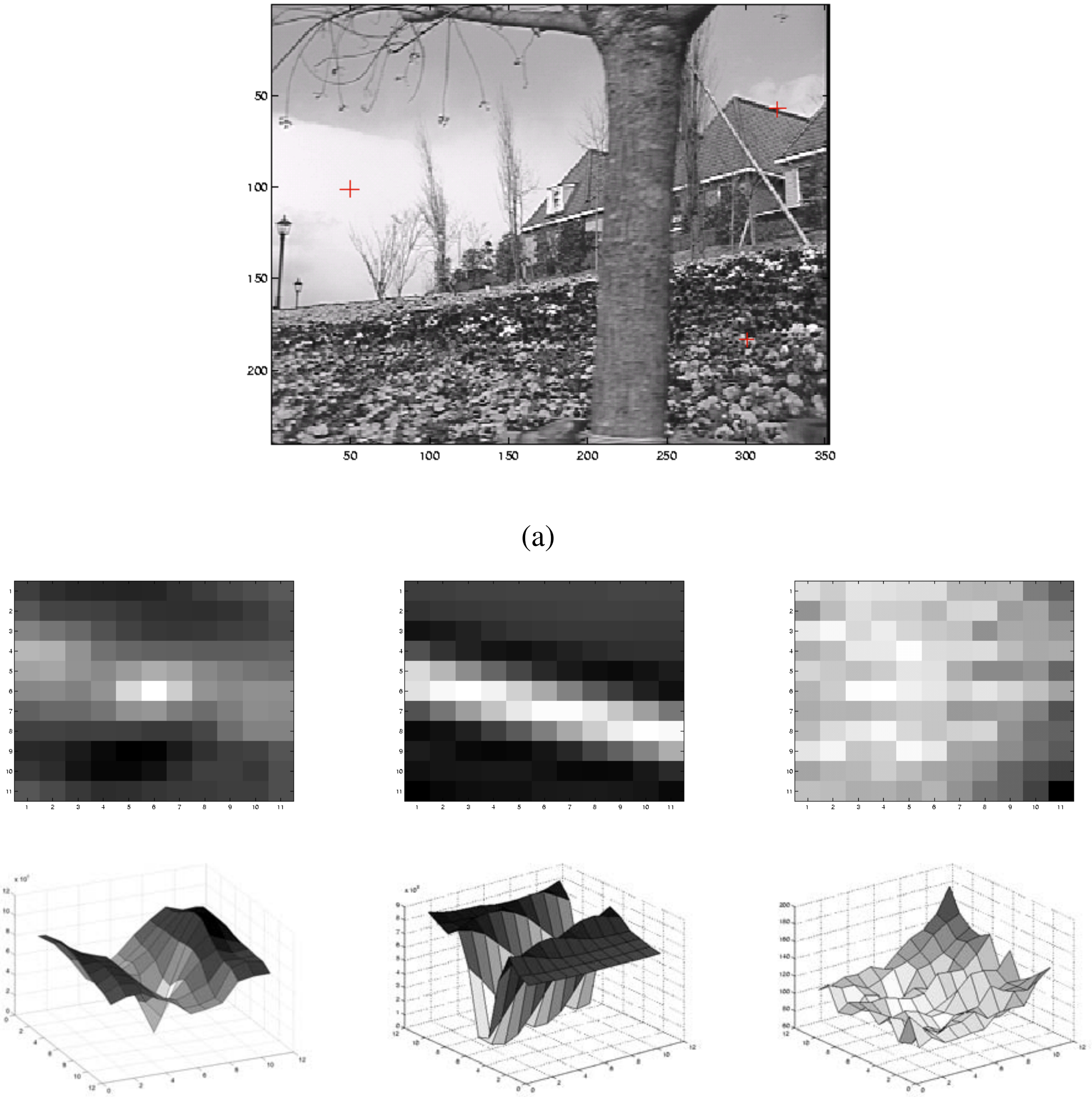

(a)

(b)

(c)

(d)

Figure 4.5: *Three different auto-correlation surfaces (b–d) shown as both grayscale images and surface plots. The original image (a) is marked with three red crosses to denote where these auto-correlation surfaces were computed. Patch (b) is from the flower bed (good unique minimum), patch (c) is from the roof edge (one-dimensional aperture problem), and patch (d) is from the cloud (no good peak).*

cross in the lower right-hand quadrant of Figure 4.5a) exhibits a strong minimum, indicating that it can be well localized. The correlation surface corresponding to the roof edge (Figure 4.5c) has a strong ambiguity along one direction, while the correlation surface corresponding to the cloud region (Figure 4.5d) has no stable minimum.

Using a Taylor Series expansion of the image function $I_0(\boldsymbol{x}_i + \Delta \boldsymbol{u}) \approx I_0(\boldsymbol{x}_i) + \nabla I_0(\boldsymbol{x}_i) \cdot \Delta \boldsymbol{u}$ (Lucas and Kanade 1981, Shi and Tomasi 1994), we can approximate the auto-correlation surface as

$$\begin{aligned} E_{\text{AC}}(\Delta \boldsymbol{u}) &= \sum_i w(\boldsymbol{x}_i)[I_0(\boldsymbol{x}_i + \Delta \boldsymbol{u}) - I_0(\boldsymbol{x}_i)]^2 && (4.3) \\ &\approx \sum_i w(\boldsymbol{x}_i)[I_0(\boldsymbol{x}_i) + \nabla I_0(\boldsymbol{x}_i) \cdot \Delta \boldsymbol{u} - I_0(\boldsymbol{x}_i)]^2 && (4.4) \\ &= \sum_i w(\boldsymbol{x}_i)[\nabla I_0(\boldsymbol{x}_i) \cdot \Delta \boldsymbol{u}]^2 && (4.5) \\ &= \Delta \boldsymbol{u}^T \boldsymbol{A} \Delta \boldsymbol{u}, && (4.6) \end{aligned}$$

where

$$\nabla I_0(\boldsymbol{x}_i) = (\frac{\partial I_0}{\partial x}, \frac{\partial I_0}{\partial y})(\boldsymbol{x}_i) \tag{4.7}$$

is the *image gradient* at $\boldsymbol{x}_i$. This gradient can be computed using a variety of techniques (Schmid *et al.* 2000). The classic “Harris” detector (Harris and Stephens 1988) uses a [-2 -1 0 1 2] filter, but more modern variants (Schmid *et al.* 2000, Triggs 2004) convolve the image with horizontal and vertical derivatives of a Gaussian (typically with $\sigma = 1$). *[Note: Bill Triggs doubts that Harris and Stephens (1988) used such a bad filter kernel, as reported in (Schmid* et al. *2000), but the original publication is hard to find.]*

The auto-correlation matrix $\boldsymbol{A}$ can be written as

$$\boldsymbol{A} = w * \begin{bmatrix} I_x^2 & I_x I_y \\ I_x I_y & I_y^2 \end{bmatrix}, \tag{4.8}$$

where we have replaced the weighted summations with discrete convolutions with the weighting kernel w. This matrix can be interpreted as tensor (multiband) image, where the outer products of the gradients ∇I are convolved with a weighting function w to provide a per-pixel estimate of the local (quadratic) shape of the auto-correlation function. In more detail, the computation of image that contains a 2×2 matrix $\boldsymbol{A}$ at each pixel can be performed in two steps:

1. At each pixel, compute the gradient $\nabla I = \begin{bmatrix} I_x & I_y \end{bmatrix}$ and then compute the four values $\begin{bmatrix} I_x^2 & I_x I_y & I_x I_y & I_y^2 \end{bmatrix}$;

2. Convolve the resulting 4-band image with a blur kernel w.

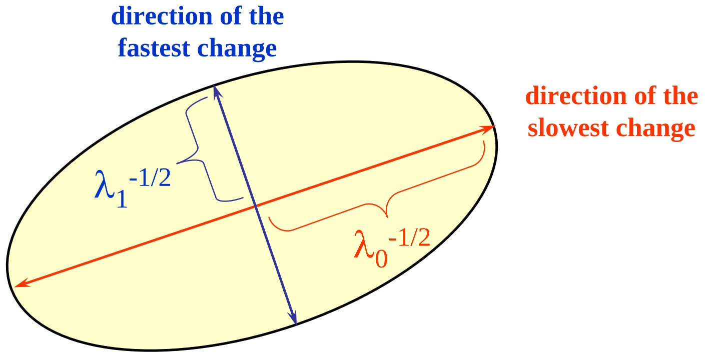
direction of the fastest change
direction of the slowest change
$\lambda_1^{-1/2}$
$\lambda_0^{-1/2}$

Figure 4.6: *Uncertainty ellipse corresponding to an eigenvalue analysis of the auto-correlation matrix* $\boldsymbol{A}$*.*

As first shown by Anandan (1984, 1989) and further discussed in §8.1.3 and (8.43), the inverse of the matrix $\boldsymbol{A}$ provides a lower bound on the uncertainty in the location of a matching patch. It is therefore a useful indicator of which patches can be reliably matched. The easiest way to visualize and reason about this uncertainty is to perform an eigenvalue analysis of the auto-correlation matrix $\boldsymbol{A}$, which produces two eigenvalues (λ_0, λ_1) and two eigenvector directions (Figure 4.6). Since the larger uncertainty depends on the smaller eigenvalue, i.e., $\lambda_0^{-1/2}$, it makes sense to find maxima in the smaller eigenvalue to locate *good features to track* (Shi and Tomasi 1994).

Förstner-Harris. While Anandan as well as Lucas and Kanade (1981) were the first to analyze the uncertainty structure of the auto-correlation matrix, they did so in the context of associating certainties with optic flow measurements. Förstner (1986) and Harris and Stephens (1988) were the first to propose using local maxima in rotationally invariant scalar measures derived from the auto-correlation matrix to locate keypoints for the purpose of sparse feature matching. (See (Schmid *et al.* 2000, Triggs 2004) for more detailed historical reviews of feature detection algorithms) Both of these techniques also proposed using a Gaussian weighting window instead of the previously used square patches, which makes the detector response insensitive to in-plane image rotations. *[Note: Decide if (Förstner 1994) is worth citing as well.]*

The minimum eigenvalue λ_0 (Shi and Tomasi 1994) is not the only quantity that can be used to find keypoints. A simpler quantity, proposed by Harris and Stephens (1988) is

$$\det(\boldsymbol{A}) - \alpha\,\mathrm{trace}(\boldsymbol{A})^2 = \lambda_0\lambda_1 - \alpha(\lambda_0 + \lambda_1)^2 \tag{4.9}$$

with $\alpha = 0.06$. *[Note: Brown* et al. *(2005) say that* $\alpha = 0.04$*. Check out the original paper.]* Unlike eigenvalue analysis, this quantity does not require the use of square roots, and yet is still rotationally invariant and also downweights edge-like features where $\lambda_1 \gg \lambda_0$. Triggs (2004)

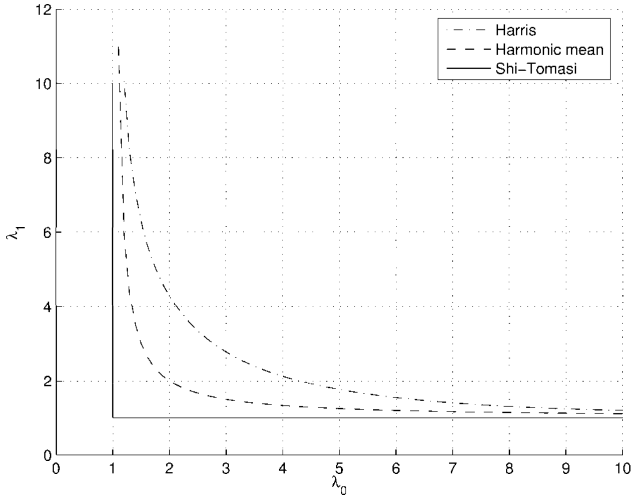

Figure 4.7: *Isocontours of popular keypoint detection functions (Brown* et al. *2004). Each detector looks for points where the eigenvalues λ_0, λ_1 of $\boldsymbol{A} = w * \nabla I \nabla I^T$ are both large.*

suggest using the quantity

$$\lambda_0 - \alpha\lambda_1 \tag{4.10}$$

(say with $\alpha = 0.05$), which also reduces the response at 1D edges, where aliasing errors sometimes inflate the smaller eigenvalue. He also shows how the basic 2 × 2 Hessian can be extended to parametric motions to detect points that are also accurately localizable in scale and rotation. Brown *et al.* (2005), on the other hand, use the harmonic mean,

$$\frac{\det \boldsymbol{A}}{\operatorname{tr} \boldsymbol{A}} = \frac{\lambda_0\lambda_1}{\lambda_0 + \lambda_1}, \tag{4.11}$$

which is a smoother function in the region where $\lambda_0 \approx \lambda_1$. Figure 4.7 shows isocontours of the various interest point operators (note that all the detectors require both eigenvalues to be large).

[Note: Decide whether to turn this into a boxed Algorithm.] The steps in the basic auto-correlation-based keypoint detector can therefore be summarized as follows:

1. Compute the horizontal and vertical derivatives of the image I_x and I_y by convolving the original image with derivatives of Gaussians §3.2.1.

2. Compute the three images corresponding to the outer products of these gradients (the matrix $\boldsymbol{A}$ is symmetric, so only three entries are needed).

3. Convolve each of these images with a larger Gaussian.

4. Compute a scalar interest measure using one of the formulas discussed above.

Note: Sample image

(a)

Note: Harris response

(b)

Note: DoG response

(c)

Figure 4.8: *Sample image (a) and two different interest operator responses: (b) Harris; (c) DoG. Local maxima are shown as red dots.*
[Note: Need to generate this figure.]

5. Find local maxima above a certain threshold and report these as detected feature point locations.

Figure 4.8 shows the resulting interest operator responses for the classic Harris detector as well as the DoG detector discussed below.

Adaptive non-maximal suppression While most feature detectors simply look for local maxima in the interest function, this can lead to an uneven distribution of feature points across the image, e.g., points will be denser in regions of higher contrast. To mitigate this problem, Brown *et al.* (2005) only detect features that are both local maxima and whose response value is significantly (10%) greater than than of all of its neighbors within a radius r (Figure 4.9c–d). They devise an efficient way to associate suppression radii with all local maxima by first sorting all local maxima by their response strength, and then creating a second list sorted by decreasing suppression radius (see (Brown *et al.* 2005) for details). A qualitative comparison of selecting the top n features vs. ANMS is shown in Figure 4.9.

Measuring repeatability Given the large number of feature detectors that have been developed in computer vision, how can we decide which ones to use? Schmid *et al.* (2000) were the first to propose measuring the *repeatability* of feature detectors, which is defined as the frequency with which keypoints detected in one image are found within ϵ (say $\epsilon = 1.5$) pixels of the corresponding location in a transformed image. In their paper, they transform their planar images by applying rotations, scale changes, illumination changes, viewpoint changes, and adding noise. They also measure the *information content* available at each detected feature point, which they define as the entropy of a set of rotationally invariant local grayscale descriptors. Among the techniques they

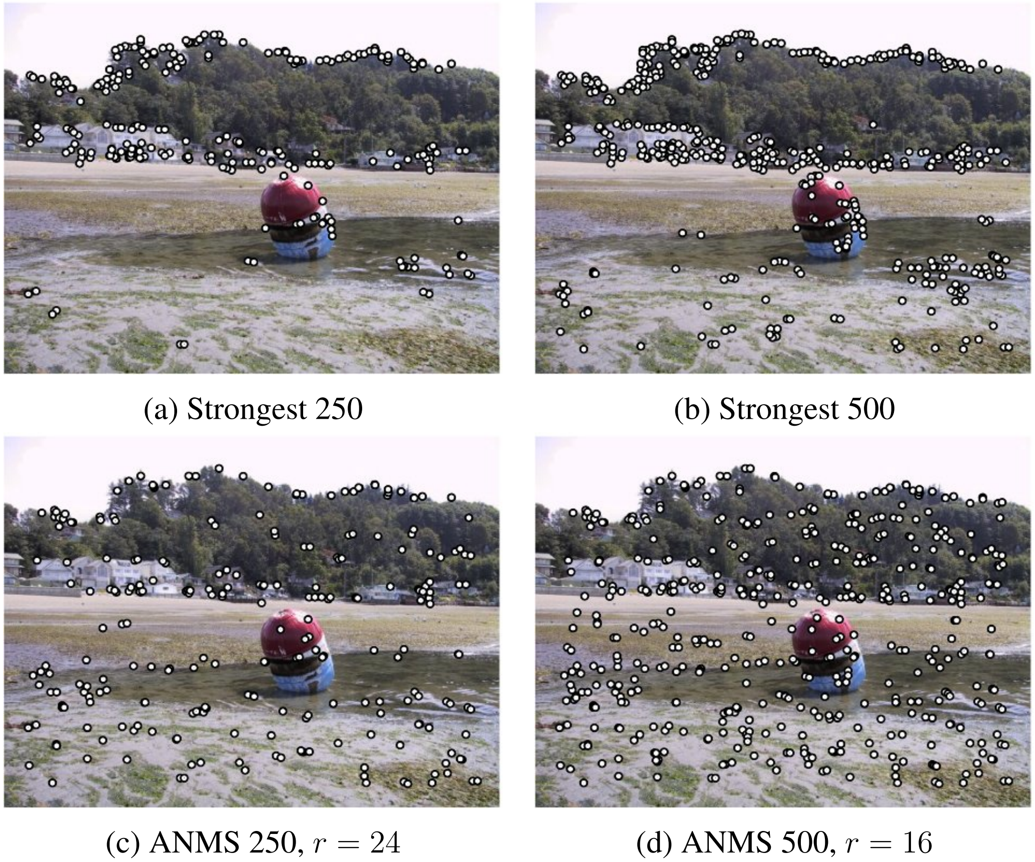
(a) Strongest 250

(b) Strongest 500

(c) ANMS 250, $r = 24$

(d) ANMS 500, $r = 16$

Figure 4.9: *Adaptive non-maximal suppression (ANMS) (Brown et al. 2005). The two upper images show the strongest 250 and 500 interest points, while the lower two images show the interest points selected with adaptive non-maximal suppression (along with the corresponding suppression radius r). Note how the latter features have a much more uniform spatial distribution across the image.*

survey, they find that the improved (Gaussian derivative) version of the Harris operator with $\sigma_d = 1$ (scale of the derivative Gaussian) and $\sigma_i = 2$ (scale of the integration Gaussian) works best.

Scale invariance

In many situations, detecting features at the finest stable scale possible may not be appropriate. For example, when matching images with little high frequency (e.g., clouds), fine-scale features may not exist.

One solution to the problem is to extract features at a variety of scales, e.g., by performing the same operations at multiple resolutions in a pyramid and then matching features at the same level. This kind of approach is suitable when the images being matched do not undergo large

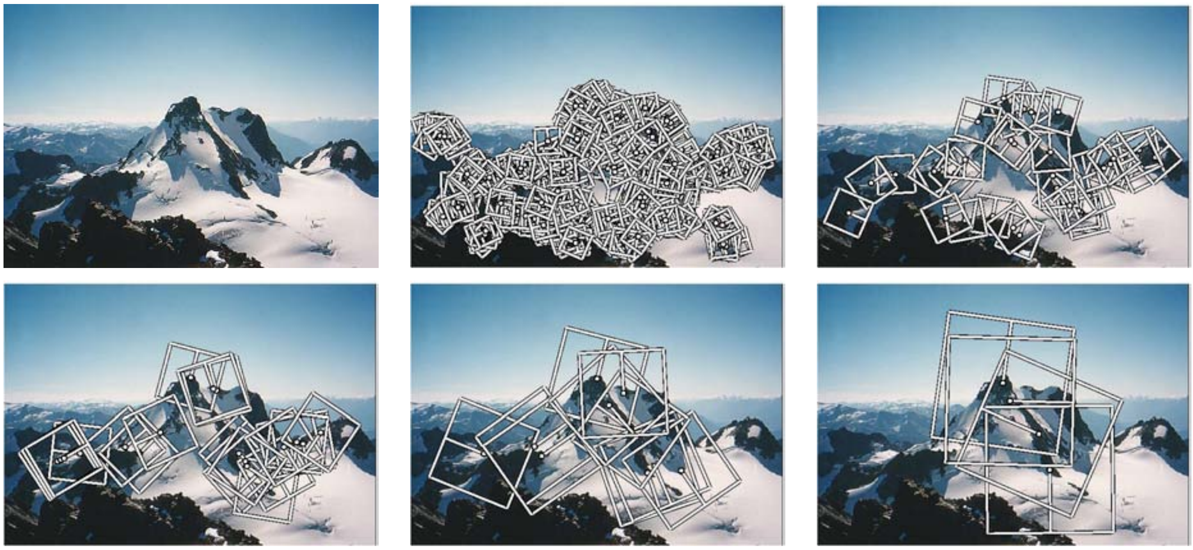

Figure 4.10: *Multi-scale Oriented Patches (MOPS) extracted at five pyramid levels (Brown* et al. *2004). The boxes show the feature orientation and the region from which the descriptor vectors are sampled.*

scale changes, e.g., when matching successive aerial images taken from an airplane, or stitching panoramas taken with a fixed focal length camera. Figure 4.10 shows the output of one such approach, the multi-scale oriented patch detector of Brown *et al.* (2005), for which responses at 5 different scales are shown.

However, for most object recognition applications, the scale of the object in the image is unknown. Instead of extracting features at many different scales and them matching all of these, it is more efficient to extract features that are stable in both location *and* scale (Lowe 2004, Mikolajczyk and Schmid 2004).

Early investigations into scale selection were performed by Lindeberg (1993, 1998b), who first proposed using extrema in the Laplacian of Gaussian (LoG) function as interest point locations. Based on this work, Lowe (2004) proposed computing a set of sub-octave Difference of Gaussian filters (Figure 4.11a), looking for 3D (space+scale) maxima in the resulting structure (Figure 4.11), and then computing a sub-pixel space+scale location using a quadratic fit (Brown and Lowe 2002). The number of sub-octave levels was chosen after careful empirical investigation, and was determined to be 3, which corresponds to a quarter-octave pyramid (the same as used by Triggs (2004)).

As with the Harris operator, pixels where there is strong asymmetry in the local curvature of the indicator function (in this case the DoG) are rejected. This is implemented by first computing

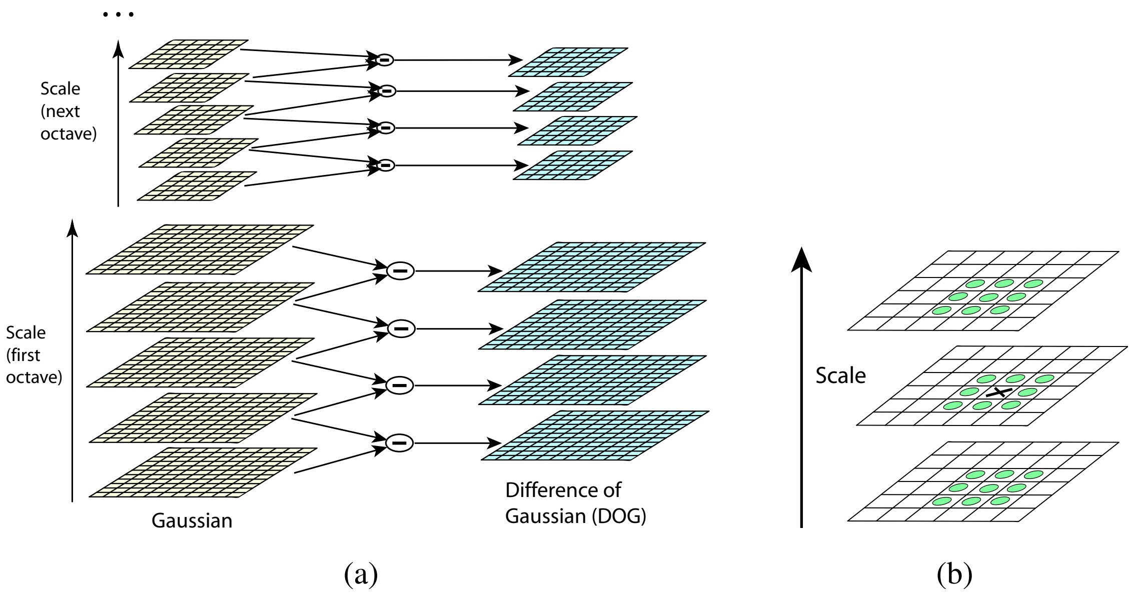

Figure 4.11: *Scale-space feature detection using a sub-octave Difference of Gaussian pyramid (Lowe 2004). (a) Adjacent levels of a sub-octave Gaussian pyramid are subtracted to produce Difference of Gaussian images. (b) Extrema (maxima and minima) in the resulting 3D volume are detected by comparing a pixel to its 26 neighbors.*

the local Hessian of the difference image D,

$$\boldsymbol{H} = \begin{bmatrix} D_{xx} & D_{xy} \\ D_{xy} & D_{yy} \end{bmatrix}, \tag{4.12}$$

and then rejecting keypoints for which

$$\frac{\text{Tr}(\boldsymbol{H})^2}{\text{Det}(\boldsymbol{H})} > 10. \tag{4.13}$$

While Lowe's Scale Invariant Feature Transform (SIFT) performs well in practice, it is not based on the same theoretical foundation of maximum spatial stability as the auto-correlation-based detectors. (In fact, its detection locations are often complementary to those produced by such techniques and can therefore be used in conjunction with these other approaches.) In order to add a scale selection mechanism to the Harris corner detector, Mikolajczyk and Schmid (2004) evaluate the Laplacian of a Gaussian function at each detected Harris point (in a multi-scale pyramid) and keep only those points for which the Laplacian is extremal (larger or smaller than both its coarser and finer-level values). An optional iterative refinement for both scale and position is also proposed and evaluated. Additional examples of scale invariant region detectors can be found in (Mikolajczyk *et al.* 2005, Tuytelaars and Mikolajczyk 2007).

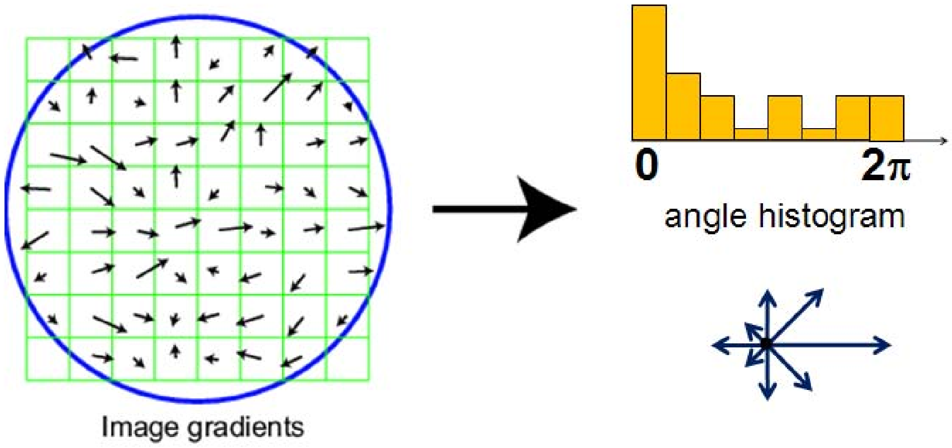

Figure 4.12: *A dominant orientation estimate can be computed by creating a histogram of all the gradient orientations (weighted by their magnitudes and/or after thresholding out small gradients), and then finding the significant peaks in this distribution (Lowe 2004).*

Rotational invariance and orientation estimation

In addition to dealing with scale changes, most image matching and object recognition algorithms need to deal with (at least) in-plane image rotation. One way to deal with this problem is to design descriptors that are rotationally invariant (Schmid and Mohr 1997), but such descriptors have poor discriminability, i.e. they map different looking patches to the same descriptor.

A better method is to estimate a *dominant orientation* at each detected keypoint. Once the local orientation and scale of a keypoint have been estimated, a scaled and oriented patch around the detected point can be extracted and used to form a feature descriptor (Figures 4.10 and 4.17).

The simplest possible orientation estimate is the average gradient within a region around the keypoint. If a Gaussian weighting function is used (Brown *et al.* 2005), this average gradient is equivalent to a first order steerable filter §3.2.1, i.e., it can be computed using an image convolution with the horizontal and vertical derivatives of Gaussian filter (Freeman and Adelson 1991). In order to make this estimate more reliable, it use usually preferable to use a larger aggregation window (Gaussian kernel size) than the detection window size (Brown *et al.* 2005). The orientations of the square boxes shown in Figure 4.10 were computed using this technique.

Sometime, however, the averaged (signed) gradient in a region can be small and therefore an unreliable indicator of orientation. A better technique in this case is to look at the *histogram* of orientations computed around the keypoint. Lowe (2004) computes a 36-bin histogram of edge orientations weighted by both gradient magnitude and Gaussian distance to the center, finds all peaks within 80% of the global maximum, and then computes a more accurate orientation estimate

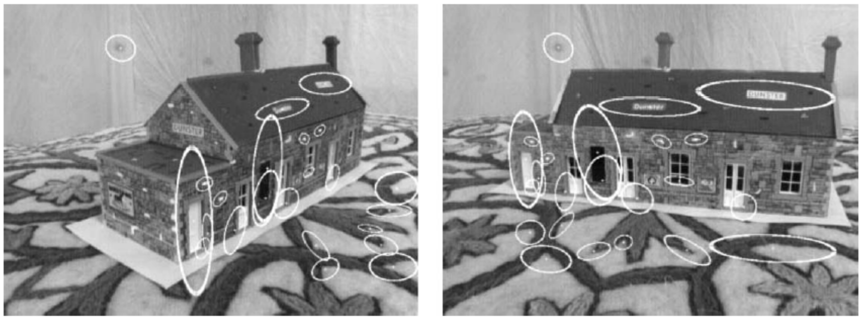

Figure 4.13: *An example of using affine region detectors to match two images taken from dramatically different viewpoints (Mikolajczyk and Schmid 2004).*

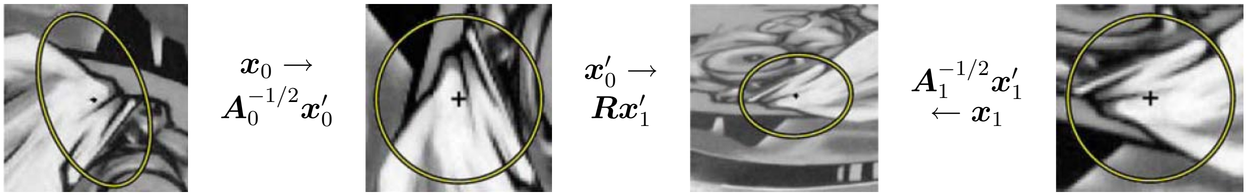
$\boldsymbol{x}_0 \rightarrow \boldsymbol{A}_0^{-1/2}\boldsymbol{x}'_0$
$\boldsymbol{x}'_0 \rightarrow \boldsymbol{R}\boldsymbol{x}'_1$
$\boldsymbol{A}_1^{-1/2}\boldsymbol{x}'_1 \leftarrow \boldsymbol{x}_1$

Figure 4.14: *Affine normalization using the second moment matrices, as described in (Mikolajczyk and Schmid 2004). After image coordinates are transformed using the matrices $\boldsymbol{A}_0^{-1/2}$ and $\boldsymbol{A}_1^{-1/2}$, they are related by a pure rotation $\boldsymbol{R}$, which can be estimated using a dominant orientation technique.*

using a 3-bin parabolic fit (Figure 4.12).

Affine invariance

While scale and rotation invariance are highly desirable, for many applications such as *wide baseline stereo matching* (Pritchett and Zisserman 1998, Schaffalitzky and Zisserman 2002) or location recognition (Chum *et al.* 2007), full affine invariance is preferred. Affine invariant detectors not only respond at consistent locations after scale and orientation changes, they also respond consistently across affine deformations such as (local) perspective foreshortening (Figure 4.13). In fact, for a small enough patch, any continuous image warping can be well approximated by an affine deformation. *[Note: Strictly speaking, detectors are defined as* covariant *if their response to a transformed image is a transform of the original response. Svetlana Lazebnik puts this nicely in slide 60 of lec07_corner_blob.ppt as features(transform(image)) = transform(features(image)). See if you can find a reference to this and explain it better.]*

To introduce affine invariance, several authors have proposed fitting an ellipse to the autocorrelation or Hessian matrix (using eigenvalue analysis) and then using the principal axes and

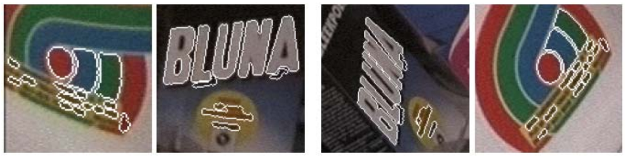

Figure 4.15: *Maximally Stable Extremal Regions (MSERs) extracted and matched from a number of images (Matas* et al. *2004).*

ratios of this fit as the affine coordinate frame (Lindeberg and Gøarding 1997, Baumberg 2000, Mikolajczyk and Schmid 2004, Mikolajczyk *et al.* 2005, Tuytelaars and Mikolajczyk 2007). Figure 4.14 shows how the square root of the moment matrix can be use to transform local patches into a frame which is similar up to rotation. *[Note: May need to fix up the above description.]*

Another important affine invariant region detector is the Maximally Stable Extremal Region (MSER) detector developed by Matas *et al.* (2004). To detect MSERs, binary regions are computed by thresholding the image at all possible gray levels (the technique therefore only works for grayscale images). This can be performed efficiently by first sorting all pixels by gray value, and then incrementally adding pixels to each connected component as the threshold is changed (Nistér and Stewénius 2008). The area of each component (region) is monitored as the threshold is changed. Regions whose rate of change of area w.r.t. threshold is minimal are defined as *maximally stable* and are returned as detected regions. This results in regions that are invariant to both affine geometric and photometric (linear bias-gain or smooth monotonic) transformations (Figure 4.15). If desired, an affine coordinate frame can be fit to each detected region using its moment matrix.

The area of feature point detectors and descriptors continues to be very active, with papers appearing every year at major computer vision conferences (Xiao and Shah 2003, Koethe 2003, Carneiro and Jepson 2005, Kenney *et al.* 2005, Bay *et al.* 2006, Platel *et al.* 2006, Rosten and Drummond 2006). Mikolajczyk *et al.* (2005) survey a number of popular affine region detectors and provide experimental comparisons of their invariance to common image transformations such as scaling, rotations, noise, and blur. These experimental results, code, and pointers to the surveyed papers can be found on their Web site at `http://www.robots.ox.ac.uk/vgg/research/affine`.

[Note: Clean up the rest of this section. Can I get some suggestions from reviewers as to which are most important?] Of course, keypoints are not the only kind of features that can be used for registering images. Zoghlami *et al.* (1997) use line segments as well as point-like features to estimate homographies between pairs of images, whereas (Bartoli *et al.* 2004) use line segments with local correspondences along the edges to extract 3D structure and motion. *[Note: Check out (Schmid and Zisserman 1997) and see what they do.]* Tuytelaars and Van Gool (2004) use affine invariant regions to detect correspondences for wide baseline stereo matching, whereas Kadir *et*

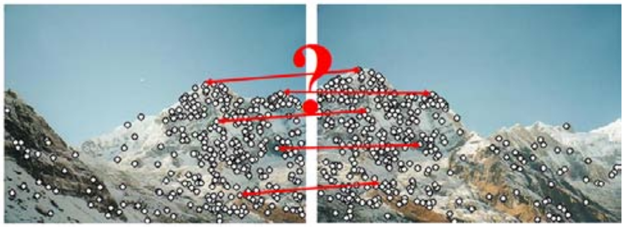

Figure 4.16: *Feature matching: how can we extract local descriptors that are invariant to inter-image variations and yet still discriminative enough to establish correct correspondences?*

al. (2004) detect salient regions where patch entropy and its rate of change with scale are locally maximal. (Corso and Hager (2005) use a related technique to fit 2D oriented Gaussian kernels to homogeneous regions.) *[Note: The following text is from Matas' BMVC 2002 paper:* Since the influential paper by Schmid and Mohr [11] many image matching and wide-baseline stereo algorithms have been proposed, most commonly using Harris interest points as distinguished regions. Tell and Carlsson [13] proposed a method where line segments connecting Harris interest points form measurement regions. The measurements are characterized by scale invariant Fourier coefficients. The Harris interest detector is stable over a range of scales, but defines no scale or affine invariant measurement region. Baumberg [1] applied an iterative scheme originally proposed by Lindeberg and Garding to associate affine-invariant measurement regions with Harris interest points. In [7], Mikolajczyk and Schmid show that a scale-invariant MR can be found around Harris interest points. In [9], Pritchett and Zisserman form groups of line segments and estimate local homographies using parallelograms as measurement regions. Tuytelaars and Van Gool introduced two new classes of affine-invariant distinguished regions, one based on local intensity extrema [16] the other using point and curve features [15]. In the latter approach, DRs are characterized by measurements from inside an ellipse, constructed in an affine invariant manner. Lowe [6] describes the "Scale Invariant Feature Transform" approach which produces a scale and orientation-invariant characterization of interest points. *]*

More details on techniques for finding and matching curves, lines, and regions, can be found in subsequent sections of this chapter.

4.1.2 Feature descriptors

After detecting the features (keypoints), we must *match* them, i.e., determine which features come from corresponding locations in different images. In some situations, e.g., for video sequences (Shi and Tomasi 1994) or for stereo pairs that have been *rectified* (Zhang *et al.* 1995, Loop and Zhang 1999, Scharstein and Szeliski 2002), the local motion around each feature point may be mostly translational. In this case, the simple error metrics such as the *sum of squared differences* or *normalized cross-correlation*, described in §8.1, can be used to directly compare the intensities

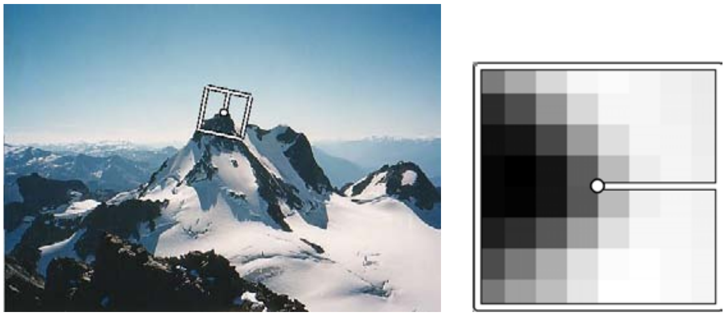

Figure 4.17: *MOPS descriptors are formed using an* 8×8 *sampling of bias/gain normalized intensity values, with a sample spacing of 5 pixels relative to the detection scale (Brown* et al. *2005). This low frequency sampling gives the features some robustness to interest point location error, and is achieved by sampling at a higher pyramid level than the detection scale.*

in small patches around each feature point. (The comparative study by Mikolajczyk and Schmid (2005) discussed below uses cross-correlation.) Because feature points may not be exactly located, a more accurate matching score can be computed by performing incremental motion refinement as described in §8.1.3, but this can be time consuming and can sometimes even decrease performance (Brown *et al.* 2005).

In most cases, however, the local appearance of features will change in orientation, scale, and even affine frame between images. Extracting a local scale, orientation, and/or affine frame estimate and then using this to resample the patch before forming the feature descriptor is thus usually preferable (Figure 4.17).

Even after compensating for these changes, the local appearance of image patches will usually still vary from image to image. How can we make the descriptor that we match more invariant to such changes, while still preserving discriminability between different (non-corresponding) patches (Figure 4.16)? Mikolajczyk and Schmid (2005) review some recently developed view-invariant local image descriptors and experimentally compare their performance. Below, we describe a few of these descriptor in more detail.

Bias and gain normalization (MOPS). For tasks that do not exhibit large amounts of foreshortening, such as image stitching, simple normalized intensity patches perform reasonably well and are simple to implement (Brown *et al.* 2005) (Figure 4.17). In order to compensate for slight inaccuracies in the feature point detector (location, orientation, and scale), these Multi-Scale Oriented Patches (MOPS) are sampled at spacing of 5 pixels relative to the detection scale (using a coarser level of the image pyramid to avoid aliasing). To compensate for affine photometric variations (linear exposure changes, *aka* bias and gain, (3.3)), patch intensities are re-scaled so that their mean is zero and their variance is one.

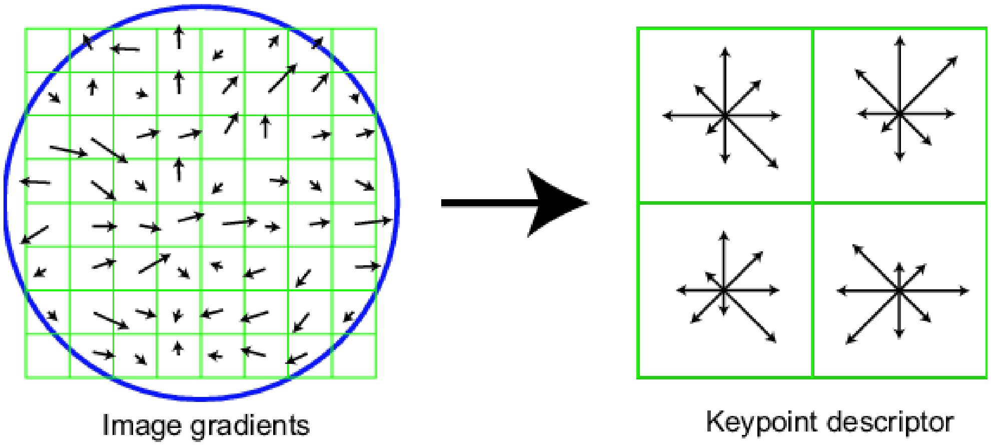

Figure 4.18: *A schematic representation of Lowe's (2004) Scale Invariant Feature Transform (SIFT). Gradient orientations and magnitudes are computed at each pixel and then weighted by a Gaussian falloff (blue circle). A weighted gradient orientation histogram is then computed in each subregion, using trilinear interpolation. While this figure shows an* 8×8 *pixel patch and a* 2×2 *descriptor array, Lowe's actual implementation uses* 16×16 *patches and a* 4×4 *array of 8-bin histograms.*

Scale Invariant Feature Transform (SIFT). SIFT features are formed by computing the gradient at each pixel in a 16×16 window around the detected keypoint, using the appropriate level of the Gaussian pyramid at which the keypoint was detected. The gradient magnitudes are downweighted by a Gaussian fall-off function (shown as a blue circle), in order to reduce the influence of gradients far from the center, as these are more affected by small misregistrations (Figure 4.18).

In each 4×4 quadrant, a gradient orientation histogram is formed by (conceptually) adding the weighted gradient value to one of 8 orientation histogram bins. To reduce the effects of location and dominant orientation misestimation, each of the original 256 weighted gradient magnitudes is softly added to $2 \times 2 \times 2$ histogram bins using trilinear interpolation. (Softly distributing values to adjacent histogram bins is generally a good idea in any application where histograms are being computed, e.g., for Hough transforms §4.3.2 or local histogram equalization §3.1.4.

The resulting 128 non-negative values form a raw version of the SIFT descriptor vector. To reduce the effects of contrast/gain (additive variations are already removed by the gradient), the 128-D vector is normalized to unit length. To further make the descriptor robust to other photometric variations, values are clipped to 0.2 and the resulting vector is once again renormalized to unit length.

PCA-SIFT Ke and Sukthankar (2004) propose a (simpler to compute) descriptor inspired by

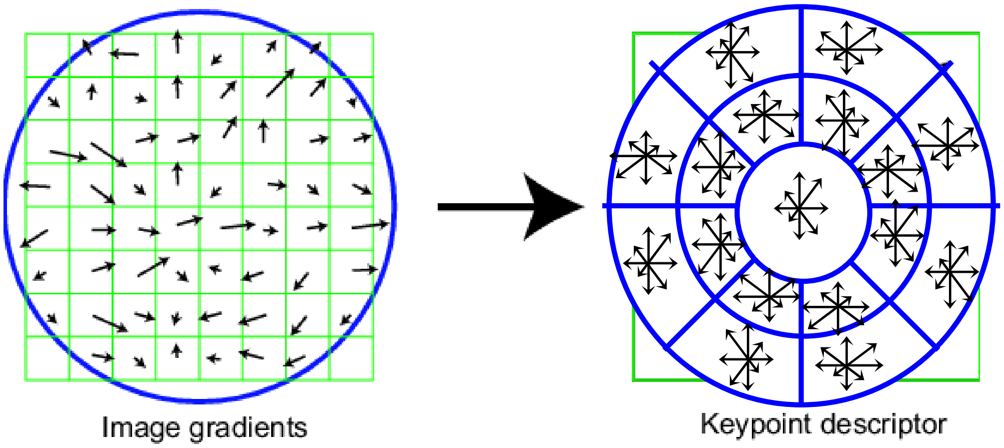

Figure 4.19: *The Gradient Location-Orientation Histogram (GLOH) descriptor uses log-polar bins instead of square bins to compute orientation histograms (Mikolajczyk and Schmid 2005). [Note: No need to get permission for this figure, I drew it myself.]*

SIFT, which computes the x and y (gradient) derivatives over a 39×39 patch and then reduces the resulting 3042-dimensional vector to 36 using PCA (Principal Component Analysis) §14.1.1, §A.1.2.

Gradient location-orientation histogram (GLOH) This descriptor, developed by Mikolajczyk and Schmid (2005), is a variant on SIFT that uses a log-polar binning structure instead of the 4 quadrants used by Lowe (2004) (Figure 4.19). The spatial bins are of radius 6, 11, and 15, with eight angular bins (except for the central region), for a total of 17 spatial bins and 16 orientation bins. The 272-dimensional histogram is then projected onto a 128 dimensional descriptor using PCA trained on a large database. In their evaluation, Mikolajczyk and Schmid (2005) found that GLOH, which has the best performance overall, outperforms SIFT by a small margin.

Steerable filters Steerable filters, §3.2.1, are combinations of derivative of Gaussian filters that permit the rapid computation of even and odd (symmetric and anti-symmetric) edge-like and corner-like features at all possible orientations (Freeman and Adelson 1991). Because they use reasonably broad Gaussians, they too are somewhat insensitive to localization and orientation errors.

Performance of local descriptors Among the local descriptors that Mikolajczyk and Schmid (2005) compared, they found that GLOH performed the best, followed closely by SIFT (Figure 4.25). Results for many other descriptors, not covered in this book, are also presented.

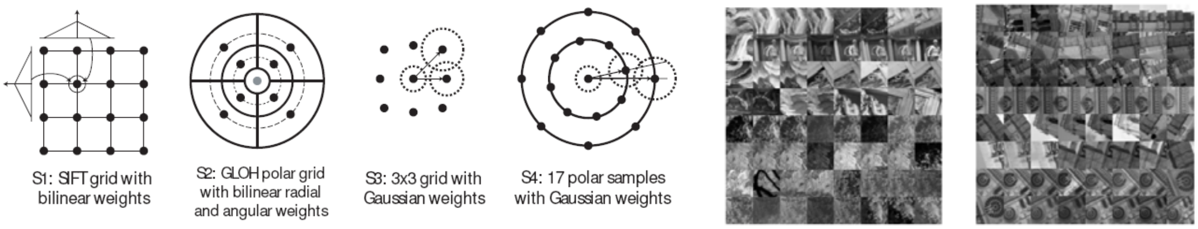
S1: SIFT grid with bilinear weights
S2: GLOH polar grid with bilinear radial and angular weights
S3: 3x3 grid with Gaussian weights
S4: 17 polar samples with Gaussian weights

(a) (b)

Figure 4.20: *Spatial summation blocks for SIFT, GLOH, and some newly developed feature descriptors (Winder and Brown 2007). The parameters for the new features (a), e.g., their Gaussian weights, are learned from a training database of matched real-world image patches (b) obtained from robust structure-from-motion applied to Internet photo collections (Hua* et al. *2007, Snavely* et al. *2006).*

The field of feature descriptors continues to evolve rapidly, with some of the newer techniques looking at local color information (van de Weijer and Schmid 2006, Abdel-Hakim and Farag 2006). Winder and Brown (2007) develop a multi-stage framework for feature descriptor computation that subsumes both SIFT and GLOH (Figure 4.20a) and also allows them to learn optimal parameters for newer descriptors that outperform previous hand-tuned descriptors. Hua *et al.* (2007) extend this work by learning lower-dimensional projections of higher-dimensional descriptors that have the best discriminative power. Both of these papers use a database of real-world image patches (Figure 4.20b) obtained by sampling images at locations that were reliably matched using a robust structure-from-motion algorithm applied to Internet photo collections (Snavely *et al.* 2006, Goesele *et al.* 2007).

While these techniques construct feature detectors that optimize for repeatability across *all* object classes, it is also possible to develop class- or instance-specific feature detectors that maximize *discriminability* from other classes (Ferencz *et al.* 2008).

4.1.3 Feature matching

Once we have extracted features and their descriptors from two or more images, the next step is to establish some preliminary feature matches between these images. The approach we take depends partially on the application, e.g., different strategies may be preferable for matching images that are known to overlap (e.g., in image stitching) vs. images that may have no correspondence whatsoever (e.g., when trying to recognize objects from a database).

In this section, we divide this problem into two separate components. The first is to select a *matching strategy*, which determines which correspondences are passed on to the next stage for further processing. The second is to devise efficient *data structures* and *algorithms* to perform

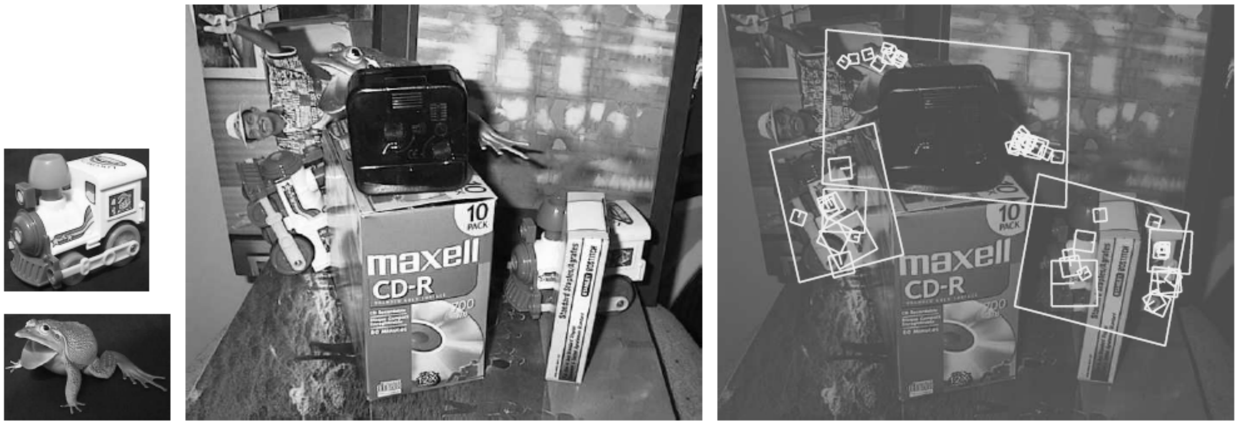

Figure 4.21: *Recognizing objects in a cluttered scene (Lowe 2004). Two of the training images in the database are shown on the left. These are matched to the cluttered scene in the middle using SIFT features, shown as small squares in the right image. The affine warp of each recognized database image onto the scene is shown as a larger parallelogram in the right image.*

this matching as quickly as possible. (See the discussion of related techniques in the chapter on recognition §14.3.2.)

Matching strategy and error rates

As we mentioned before, the determining which features matches are reasonable to further process depends on the context in which the matching is being performed. Say we are given two images that overlap to a fair amount (e.g., for image stitching, as in Figure 4.16, or for tracking objects in a video). We know that most features in one image are likely to match the other image, although some may not match because they are occluded or their appearance has changed too much.

On the other hand, if we are trying to recognize how may known objects appear in a cluttered scene (Figure 4.21), most of the features may not match. Furthermore, a large number of potentially matching objects must be searched, which requires more efficient strategies, as described below.

To begin with, we assume that the feature descriptors have been designed so that Euclidean (vector magnitude) distances in feature space can be used for ranking potential matches. If it turns out that certain parameters (axes) in a descriptor are more reliable than others, it is usually preferable to re-scale these axes ahead of time, e.g., by determining how much they vary when compared against other known good matches (Hua *et al.* 2007). (A more general process that involves transforming feature vectors into a new scaled basis is called *whitening*, and is discussed in more detail in the context of eigenface-based face recognition §14.1.1 (14.7).)

Given a Euclidean distance metric, the simplest matching strategy is to set a threshold (max-

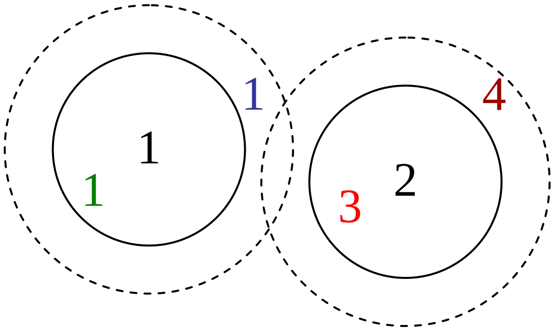

Figure 4.22: *An example of false positives and negatives. The black digits 1 and 2 are the features being matched against a database of features in other images. At the current threshold setting (black circles), the green 1 is a* true positive *(good match), the blue 1 is a* false negative *(failure to match), and the red 3 is a* false positive *(incorrect match). If we set the threshold higher (dashed circle), the blue 1 becomes a true positive, but the brown 4 becomes an additional false positive.*

imum distance) and to return all matches from other images within this threshold. Setting the threshold too high results in too many *false positives*, i.e., incorrect matches being returned. Setting the threshold too low results in too many *false negatives*, i.e., too many correct matches being missed (Figure 4.22).

We can quantify the performance of a matching algorithm at a particular threshold by first counting the number of true and false matches and match failures, using the following definitions (Fawcett 2006):

- TP: true positives, i.e., number of correct matches;
- FN: false negatives, matches that were not correctly detected;
- FP: false positives, estimated matches that are incorrect;
- TN: true negatives, non-matches that were correctly rejected.

Table 4.1 shows a sample *confusion matrix* (contingency table) containing such numbers.

We can convert these numbers into *unit rates* by defining the following quantities (Fawcett 2006):

- true positive rate TPR,

$$\text{TPR} = \frac{\text{TP}}{\text{TP+FN}} = \frac{\text{TP}}{\text{P}}; \tag{4.14}$$

- false positive rate FPR,

$$\text{FPR} = \frac{\text{FP}}{\text{FP+TN}} = \frac{\text{FP}}{\text{N}}; \tag{4.15}$$

	True matches	True non-match.		
Pred. matches	TP = 18	FP = 4	P' = 22	PPV = 0.82
Pred. non-match.	FN = 2	TN = 76	N' = 78	
	P = 20	N = 80	Total = 100	
	TPR = 0.90	FPR = 0.05		ACC = 0.94

Table 4.1: *Sample table showing the number of matches correctly and incorrectly estimated by a feature matching algorithm. The table shows the number true positives (TP), false negatives (FN), false positives (FP), true negatives (TN). The columns sum up to the actual number of positives (P) and negatives (N), while the rows sum up to the estimated number of positives (P') and negatives (N'). The formulas for the true positive rate (TPR), the false positive rate (FPR), the positive predictive value (PPR), and the accuracy (ACC) are given in the text.*

- positive predictive value (PPR),

$$\text{PPR} = \frac{\text{TP}}{\text{TP+TN}} = \frac{\text{TP}}{\text{P'}}; \tag{4.16}$$

- accuracy (ACC),

$$\text{ACC} = \frac{\text{TP+TN}}{\text{P+N}}. \tag{4.17}$$

Again, table 4.1 shows some sample numbers.

In the *information retrieval* (or document retrieval) literature, the terms *precision* is used instead of PPV (how many returned documents are relevant) and *recall* is used instead of TPR (what fraction of relevant documents was found).

Any particular matching strategy (at a particular threshold or parameter setting) can be rated by the TPR and FPR numbers: ideally, the true positive rate will be close to 1, and the false positive rate close to 0. As we vary the matching threshold, we obtain a family of such points, which are collectively known as the *Receiver Operating Characteristic* or *ROC curve* (Fawcett 2006) (Figure 4.23a). The closer this curve lies to the upper left corner, i.e., the larger the area under the curve (AUC), the better its performance. Figure 4.23b shows how we can plot the number of matches and non-matches as a function of inter-feature distance d. These curves can then be used to plot an ROC curve (Exercise 4.4).

The problem with using a fixed threshold is that it is difficult to set; the useful range of thresholds can vary a lot as we move to different parts of the feature space (Lowe 2004, Mikolajczyk and Schmid 2005). A better strategy in such cases is to simply match the *nearest neighbor* in feature space. Since some features may have no matches (e.g., they may be part of background clutter in

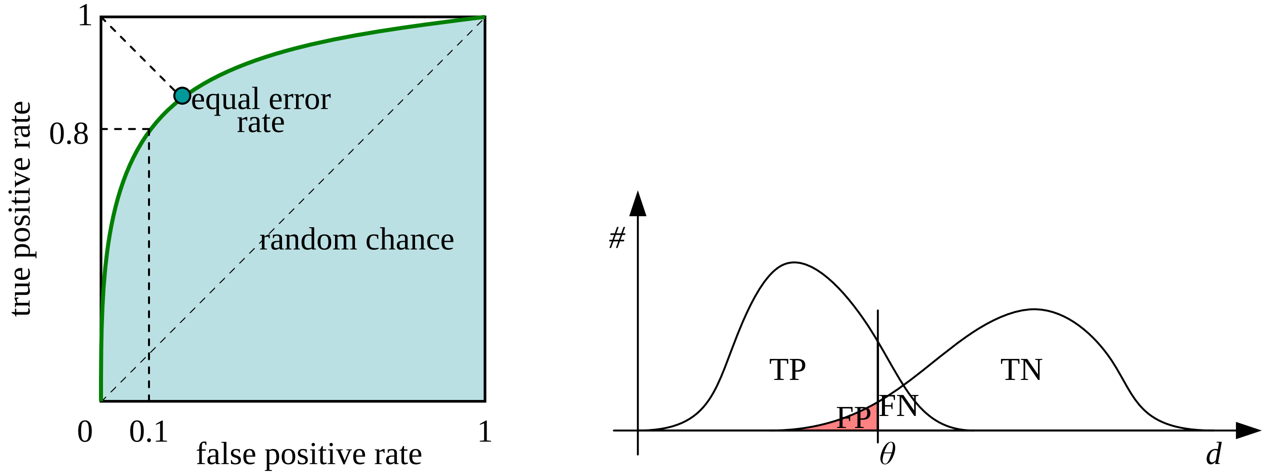

(a)

(b)

Figure 4.23: *ROC curve and its related rates. (a) The ROC curve plots the true positive rate against the false negative rate for a particular combination of feature extraction and matching algorithms. Ideally, the true positive rate should be close to 1, while the true negative rate is close to 0. The area under the ROC curve (AUC) is often used as a single (scalar) measure of algorithm performance. Alternatively, the equal error rate is sometimes used. (b) The distribution of positives (matches) and negatives (non-matches) as a function of inter-feature distance* d*. As the threshold* θ *is increased, the number of true positives (TP) and false positives (FP) increases.*

object recognition, or they may be occluded in the other image), a threshold is still used to reduce the number of false positives.

Ideally, this threshold itself will adapt to different regions of the feature space. If sufficient training data is available (Hua *et al.* 2007), it is sometimes possible to learn different thresholds for different features. Often, however, we are simply given a collection of images to match, e.g., when stitching images or constructing 3D models from unordered photo collections (Brown and Lowe 2007, Brown and Lowe 2003, Snavely *et al.* 2006). In this case, a useful heuristic can be to compare the nearest neighbor distance to that of the second nearest neighbor, preferably taken from an image that is known not to match the target (e.g., a different object in the database) (Brown and Lowe 2002, Lowe 2004). We can define this *nearest neighbor distance ratio* (Mikolajczyk and Schmid 2005) as

$$\text{NNDR} = \frac{d_1}{d_2} = \frac{\|D_A - D_B|}{\|D_A - D_C|}, \tag{4.18}$$

where d_1 and d_2 are the nearest and second nearest neighbor distances, and $D_A, \ldots, D_C$ are the target descriptor along with its closest two neighbors (Figure 4.24).

The effects of using these three different matching strategies for the feature descriptors evalu-

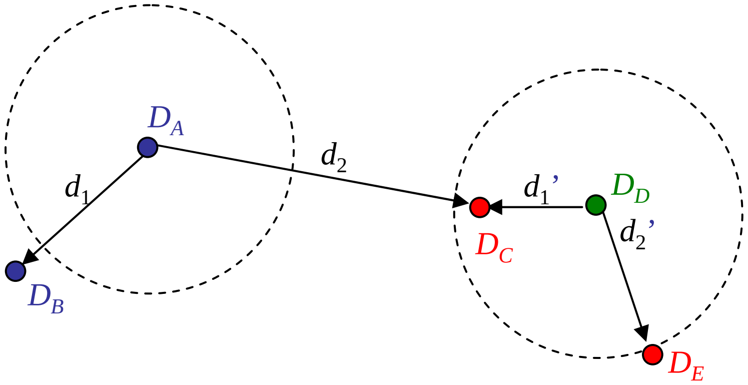

Figure 4.24: *Fixed threshold, nearest neighbor, and nearest neighbor distance ratio matching. At a fixed distance threshold (dashed circles), descriptor D_A fails to match D_B, and D_D incorrectly matches D_C and D_E. If we pick the nearest neighbor, D_A correctly matches D_B, but D_D incorrectly matches D_C. Using nearest neighbor distance ratio (NNDR) matching, the small NNDR d_1/d_2 correctly matches D_A with D_B, and the large NNDR d'_1/d'_2 correctly rejects matches for D_D.*

ated by Mikolajczyk and Schmid (2005) can be seen in Figure 4.25. As you can see, the nearest neighbor and NNDR strategies produce improved ROC curves.

Efficient matching

Once we have decided on a matching strategy, we still need to efficiently search for potential candidates. The simplest way to find all corresponding feature points is to compare all features against all other features in each pair of potentially matching images. Unfortunately, this is quadratic in the number of extracted features, which makes it impractical for most applications.

A better approach is to devise an *indexing structure* such as a multi-dimensional search tree or a hash table to rapidly search for features near a given feature. Such indexing structures can either be built for each image independently (which is useful if we want to only consider certain potential matches, e.g., searching for a particular object), or globally for all the images in a given database, which can potentially be faster, since it removes the need to iterate over each image. For extremely large databases (millions of images or more), even more efficient structures based on ideas from document retrieval (e.g., *vocabulary trees*, (Nistér and Stewénius 2006)) can be used §14.3.2.

One of the simpler techniques to implement is multi-dimensional hashing, which maps descriptors into fixed size buckets based on some function applied to each descriptor vector. At matching time, each new feature is hashed into a bucket, and a search of nearby buckets is used to return potential candidates (which can then be sorted or graded to determine which are valid matches).

A simple example of hashing is the Haar wavelets used by Brown *et al.* (2005) in their MOPS

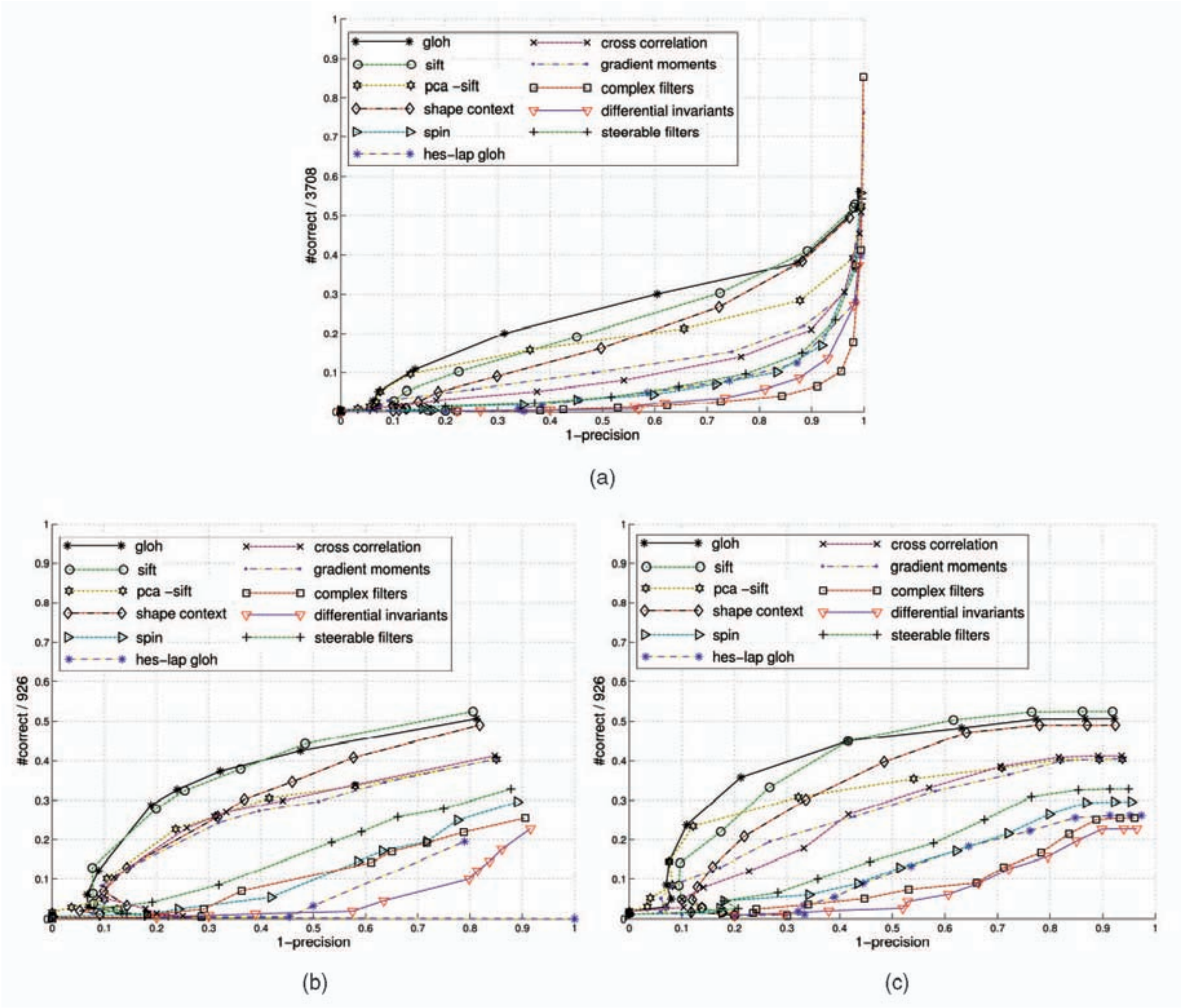

(a)

(b)

(c)

Figure 4.25: *Performance of the feature descriptors evaluated by Mikolajczyk and Schmid (2005), shown for three different matching strategies: (a) fixed threshold; (b) nearest neighbor; (c) nearest neighbor distance ratio (NNDR). Note how the ordering of the algorithms does not change that much, but the overall performance varies significantly between the different matching strategies.*

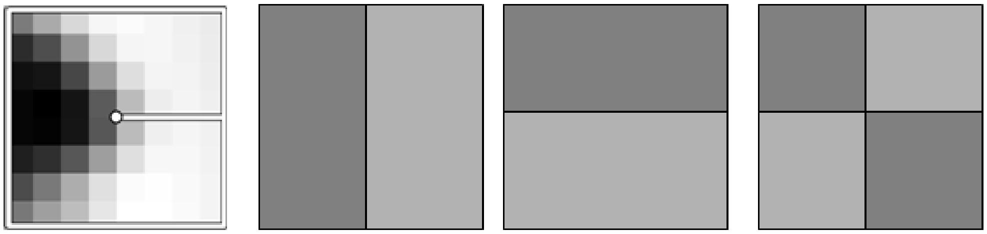

Figure 4.26: *The three Haar wavelet coefficients used for hashing the MOPS descriptor devised by Brown* et al. *(2005) are computed by summing each* 8×8 *normalized patch over the light and dark gray regions and taking their difference.*

paper. During the matching structure construction, each 8×8 scaled, oriented, and normalized MOPS patch is converted into a 3-element index by performing sums over different quadrants of the patch (Figure 4.26). The resulting three values are normalized by their expected standard deviations and then mapped to the two (of $b = 10$) nearest 1-D bins. The three-dimensional indices formed by concatenating the three quantized values are used to index the $2^3 = 8$ bins where the feature is stored (added). At query time, only the primary (closest) indices are used, so only a single three-dimensional bin needs to be examined. The coefficients in the bin can then used to select k approximate nearest neighbors for further processing (such as computing the NNDR).

A more complex, but more widely applicable, version of hashing is called *locality-sensitive hashing*, which uses unions of independently computed hashing functions to index the features (Gionis *et al.* 1999, Shakhnarovich *et al.* 2006). Shakhnarovich *et al.* (2003) extend this technique to be more sensitive to the distribution of points in parameter space, which they call *parameter-sensitive hashing*. *[Note: Even more recent work converts high-dimensional descriptor vectors into binary codes that can be compared using Hamming distances (Torralba* et al. *2008, Weiss* et al. *2008), or better LSH (Kulis and Grauman 2009). There's even the most recent NIPS submission by Lana...] [Note: Probably won't mention earlier work by Salakhutdinov and Hinton, since it's well described and compared in (Weiss* et al. *2008).]*

Another widely used class of indexing structures are multi-dimensional search trees. The best known of these are called *k-D trees*, which divide the multi-dimensional feature space along alternating axis-aligned hyperplanes, choosing the threshold along each axis so as to maximize some criterion such as the search tree balance (Samet 1989). Figure 4.27 shows an example of a two-dimensional k-d tree. Here, eight different data points A–H are shown as small diamonds arranged on a two-dimensional plane. The k-d tree recursively splits this plane along axis-aligned (horizontal or vertical) cutting planes. Each split can be denoted using the dimension number and split value (Figure 4.27b). The splits are arranged so as to try to balance the tree (keep its maximum depths as small as possible). At query time, a classic k-d tree search first locates the query point

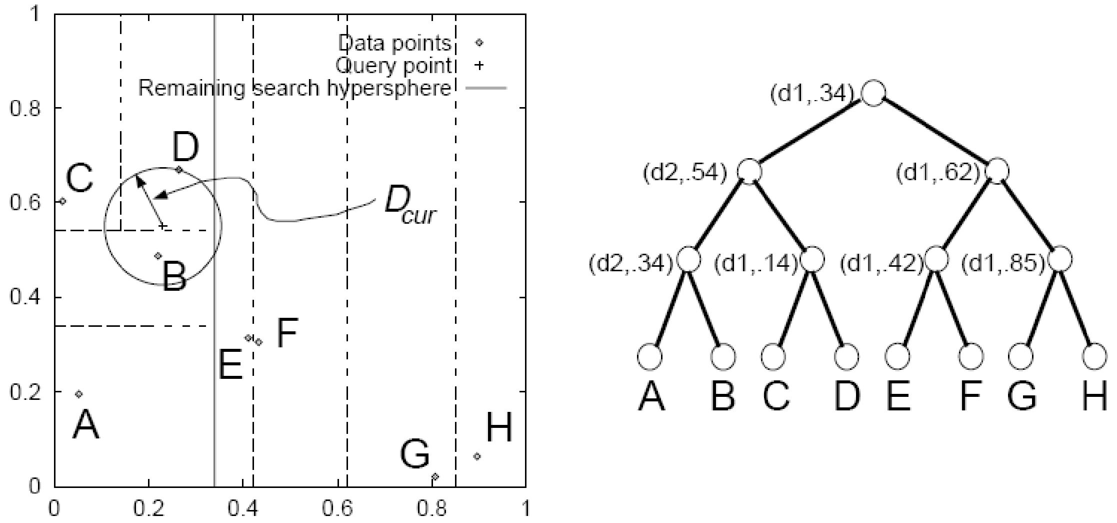

(a) (b)

Figure 4.27: *k-D tree and Best Bin First (BBF), from (Beis and Lowe 1999). (a) The spatial arrangement of the axis-aligned cutting planes is shown using dashed lines. Individual data points are shown as small diamonds. (b) The same subdivision can be represented as a tree, where each interior node represents an axis-aligned cutting plane (e.g., the top node cuts along dimension d1 at value .34), and each leaf node is a data point. During Best Bin First (BBF) search, a query point, denoted by a '+', first looks in its containing bin (D) and then in its nearest adjacent bin (B), rather than its closest neighbor in the tree (C).*

(+) in its appropriate bin (D), and then searches nearby leaves in the tree (C, B, . . .) until it can guarantee that the nearest neighbor has been found. The Best Bin First (BBF) search (Beis and Lowe 1999) searches bins in order of their spatial proximity to the query point, and is therefore usually more efficient.

Many additional data structure have been developed over the years for solving nearest neighbor problems (Arya *et al.* 1998, Liang *et al.* 2001, Hjaltason and Samet 2003). For example, Nene and Nayar (1997) developed a technique they call *slicing* that uses a series of 1D binary searches on the point list sorted along different dimensions to efficiently cull down a list of candidate points that lie within a hypercube of the query point. Grauman and Darrell (2005) re-weight the matches at different levels of an indexing tree, which allows their technique to be less sensitive to discretization errors the tree construction. Nistér and Stewénius (2006) use a *metric tree*, which consists of comparing feature descriptors to a small number of prototypes at each level in a hierarchy. The resulting quantized *visual words* can then be used with classical information retrieval (document relevance) techniques to quickly winnow down a set of potential candidates from a database of millions of images §14.3.2. Muja and Lowe (2009) compare a number of these approaches, introduce a new one of their own (priority search on hierarchical k-means trees), and conclude that multiple randomized k-d trees often provide the best performance. Despite all of this promising work, the rapid computation of image feature correspondences remains a challenging open research problem.

Feature match verification and densification

Once we have some hypothetical (putative) matches, we can often use geometric alignment §6.1 to verify which matches are *inliers* and which ones are *outliers*. For example, if we expect the whole image to be translated or rotated in the matching view, we can fit a global geometric transform and keep only those feature matches that are sufficiently close to this estimated transformation. The process of selecting a small set of seed matches and then verifying a larger set is often called *random sampling* or RANSAC §6.1.4. Once an initial set of correspondences has been established, some systems look for additional matches, e.g., by looking for additional correspondences along epipolar lines §11.1 or in the vicinity of estimated locations based on the global transform. These topics will be discussed further in Sections §6.1, §11.2, and §14.3.1.

4.1.4 Feature tracking

An alternative to independently finding features in all candidate images and then matching them is to find a set of likely feature locations in a first image and to then *search* for their corresponding locations in subsequent images. This kind of *detect then track* approach is more widely used for video tracking applications, where the expected amount of motion and appearance deformation between adjacent frames is expected to be small (or at least bounded).

The process of selecting good features to track is closely related to selecting good features for more general recognition applications. In practice, regions containing high gradients in both directions, i.e., which have high eigenvalues in the auto-correlation matrix (4.8), provide stable locations at which to find correspondences (Shi and Tomasi 1994).

In subsequent frames, searching for locations where the corresponding patch has low squared difference (4.1) often works well enough. However, if the images are undergoing brightness change, explicitly compensating for such variations (8.9) or using *normalized cross-correlation* (8.11) may be preferable. If the search range is large, it is also often more efficient to use a *hierarchical* search strategy, which uses matches in lower-resolution images to provide better initial guesses and hence speed up the search §8.1.1. Alternatives to this strategy involve *learning* what the appearance of the patch being tracked should be, and then searching for it in a vicinity of its predicted position (Avidan 2001, Jurie and Dhome 2002, Williams *et al.* 2003). These topics are all covered in more detail in the section on incremental motion estimation §8.1.3.

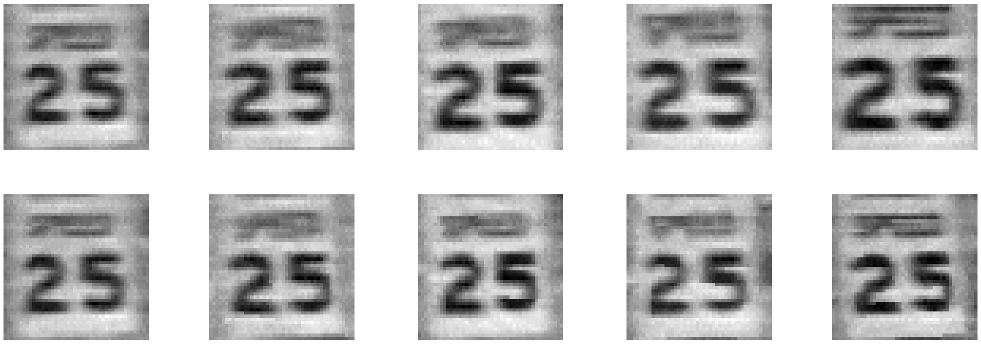

Figure 4.28: *Feature tracking using an affine motion model (Shi and Tomasi 1994). Top row: image patch around the tracked feature location. Bottom row: image patch after warping back toward the first frame using an affine deformation. Even though the speed sign gets larger from frame to frame, the affine transformation maintains a good resemblance between the original and subsequent tracked frames.*

If features are being tracked over longer image sequences, their appearance can undergo larger changes. You then have to decide whether to continue matching against the originally detected patch (feature), or to re-sample each subsequent frame at the matching location. The former strategy is prone to failure as the original patch can undergo appearance changes such as foreshortening. The latter runs the risk of the feature drifting from its original location to some other location in the image (Shi and Tomasi 1994). (Mathematically, one can argue that small mis-registration errors compound to create a *Markov Random Walk*, which leads to larger drift over time.)

A preferable solution is to compare the original patch to later image locations using an *affine* motion model §8.2. Shi and Tomasi (1994) first compare patches using a translational model between neighboring frames, and then use the location estimate produced by this step to initialize an affine registration between the patch in the current frame and the base frame where a feature was first detected (Figure 4.28). In their system, features are only detected infrequently, i.e., only in regions where tracking has failed. In the usual case, an area around the current *predicted* location of the feature is searched with an incremental registration algorithm §8.1.3.

Since their original work on feature tracking, Shi and Tomasi's approach has generated a string of interesting follow-on papers and applications. Beardsley *et al.* (1996) use extended feature tracking combined with structure from motion §7 to incrementally build up sparse 3D models from video sequences. Kang *et al.* (1997) tie together the corners of adjacent (regularly gridded) patches to provide some additional stability to the tracking (at the cost of poorer handling of occlusions). Tommasini *et al.* (1998) provide a better spurious match rejection criterion for the basic Shi and Tomasi algorithm, Collins and Liu (2003) provide improved mechanisms for feature selection and dealing with larger appearance changes over time, and Shafique and Shah (2005) develop

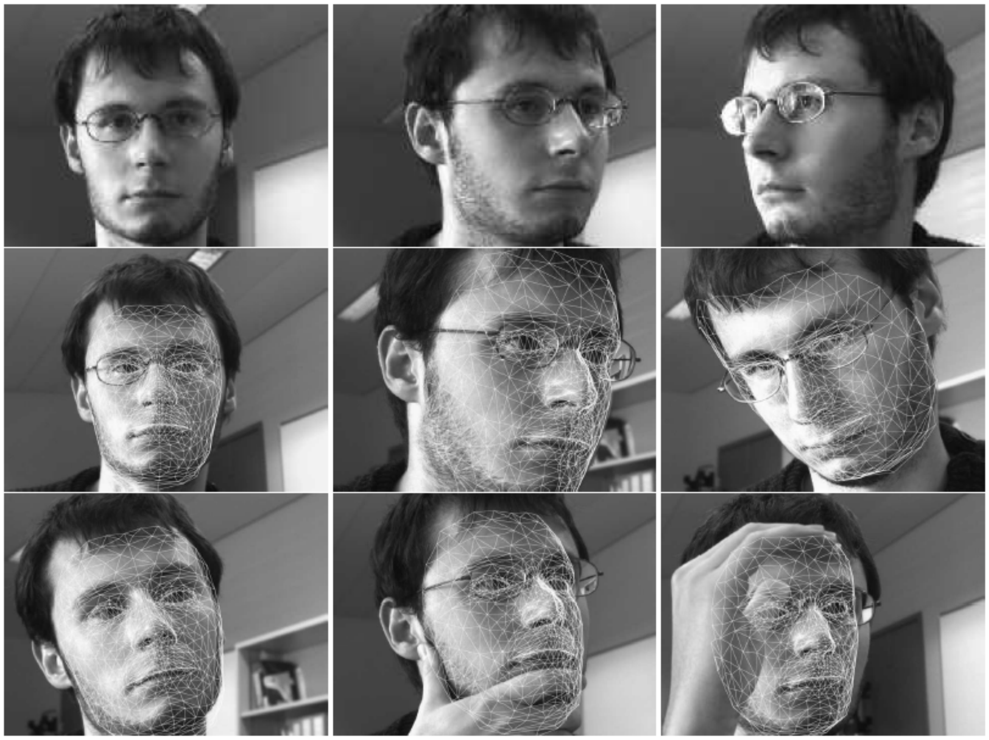

Figure 4.29: *Real-time head tracking using the fast trained classifiers of Lepetit* et al. *(2004).*

algorithms for feature matching (data association) for videos with large numbers of moving objects or points. Yilmaz *et al.* (2006) and Lepetit and Fua (2005) survey the larger field object tracking, which includes not only feature-based techniques but also alternative techniques such as contour and region-based techniques §5.1.

One of the newest developments in feature tracking is the use of learning algorithms to build special-purpose recognizers to rapidly search for matching features anywhere in an image (Lepetit *et al.* 2005, Hinterstoisser *et al.* 2008, Rogez *et al.* 2008).[2] By taking the time to train classifiers on sample patches and their affine deformations, extremely fast and reliable feature detectors can be constructed, which enables much faster motions to be supported. (Figure 4.29). Coupling such features to deformable models (Pilet *et al.* 2008) or structure-from-motion algorithms (Klein and Murray 2008) can result in even higher stability

[Note: The Lepetit and Fua (2005) survey has lots of great info and references on tracking, and also a great Mathematical Tools section. Re-read and see if I want to incorporate more, e.g., line-based 3D tracking.]

[2] See also my previous comment on earlier work in learning-based tracking (Avidan 2001, Jurie and Dhome 2002, Williams *et al.* 2003).

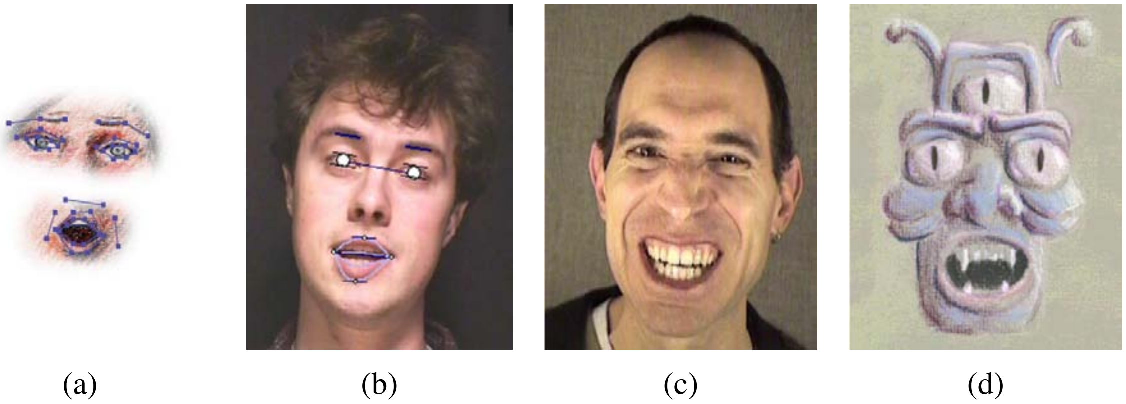

Figure 4.30: *Performance-driven hand-drawn animation (Buck* et al. *2000). (a) eye and mouth portions of hand-drawn sketch with their overlaid control lines; (b) an input video frame with the tracked features overlaid; (c) a different input video frame along with its (d) corresponding hand-drawn animation.*

4.1.5 *Application*: Performance-driven animation

One of the most compelling applications of fast feature tracking is *performance-driven animation*, i.e., the interactive deformation of a 3D graphics model based on tracking a user's motions (Williams 1990, Litwinowicz and Williams 1994, Lepetit *et al.* 2004).

Buck *et al.* (2000) present a system for tracking a user's facial expressions and head motion and using these to morph among a series of hand-drawn sketches. The system starts by extracting the eye and mouth regions of each sketch and drawing control lines over each image (Figure 4.30a). At run time, a face tracking system (see (Toyama 1998) for a survey of such systems) determines the current location of these features (Figure 4.30b). The animation system decides which input images to morph based on nearest neighbor feature appearance matching and triangular barycentric interpolation. It also computes The global location and orientation of the head from the tracked features. The resulting morphed eye and mouth regions are then composited back into the overall head model to yield a frame of hand-drawn animation (Figure 4.30d).

4.2 Edges

While interest points are useful for finding image locations that can be accurately matched in 2D, edge points are far more plentiful and often carry important semantic associations. For example, the boundaries of objects, which also correspond to occlusion events in 3D, are usually delineated by visible contours. Other kinds of edges correspond to shadow boundaries or crease edges, where surface orientation changes rapidly. "Line drawings", which consist solely of drawn contours, are

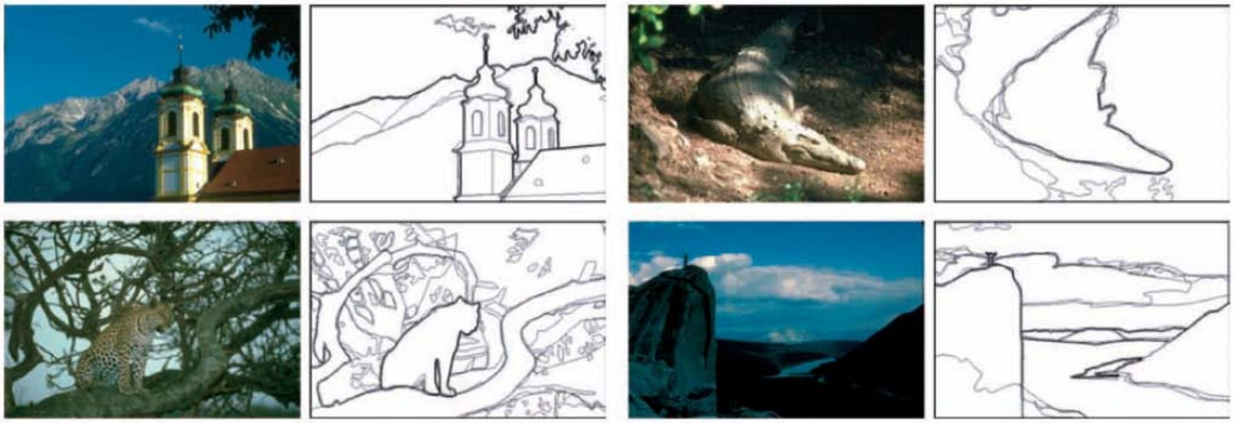

Figure 4.31: *Human boundary detection (Martin* et al. *2004). The darkness of the edges corresponds to how many human subjects marked an object boundary at that location.*

popular elements in books for infants, who seem to have no difficulty in recognizing familiar objects or animals from such simple depictions. *[Note: Find a reference from the visual perception / psychophysics literature? How about (Palmer 1999)?]* Isolated edge points can also be grouped longer *curves* or *contours*, as well as *straight line segments* §4.3.

4.2.1 Edge detection

Given an image, how can we find the salient edges? Consider the color images in Figure 4.31. If someone asked you to point out the most "salient" or "strongest" edges or the object boundaries (Martin *et al.* 2004), which ones would you trace? How closely do your perceptions match the edge images shown in Figure 4.31.

Qualitatively, edges occur at boundaries between regions of different color, intensity, or texture. Unfortunately, segmenting an image into coherent regions is a difficult task, which we will address later in §5. Often, it is preferable to detect edges using only purely local information.

Under such conditions, a reasonable approach is to define an edge as a location of *rapid intensity variation*.[3] Think of an image as a height field (Figure 4.32). On such a surface, edges occur at locations of *steep slopes*, or equivalently, in regions of closely packed contour lines (on a topographic map).

A mathematical way to define the slope (and direction) of a surface is through its gradient,

$$\boldsymbol{J}(\boldsymbol{x}) = \nabla I(\boldsymbol{x}) = (\frac{\partial I}{\partial x}, \frac{\partial I}{\partial y})(\boldsymbol{x}). \tag{4.19}$$

[3] We defer the topic of edge detection in color images to the next sub-section.

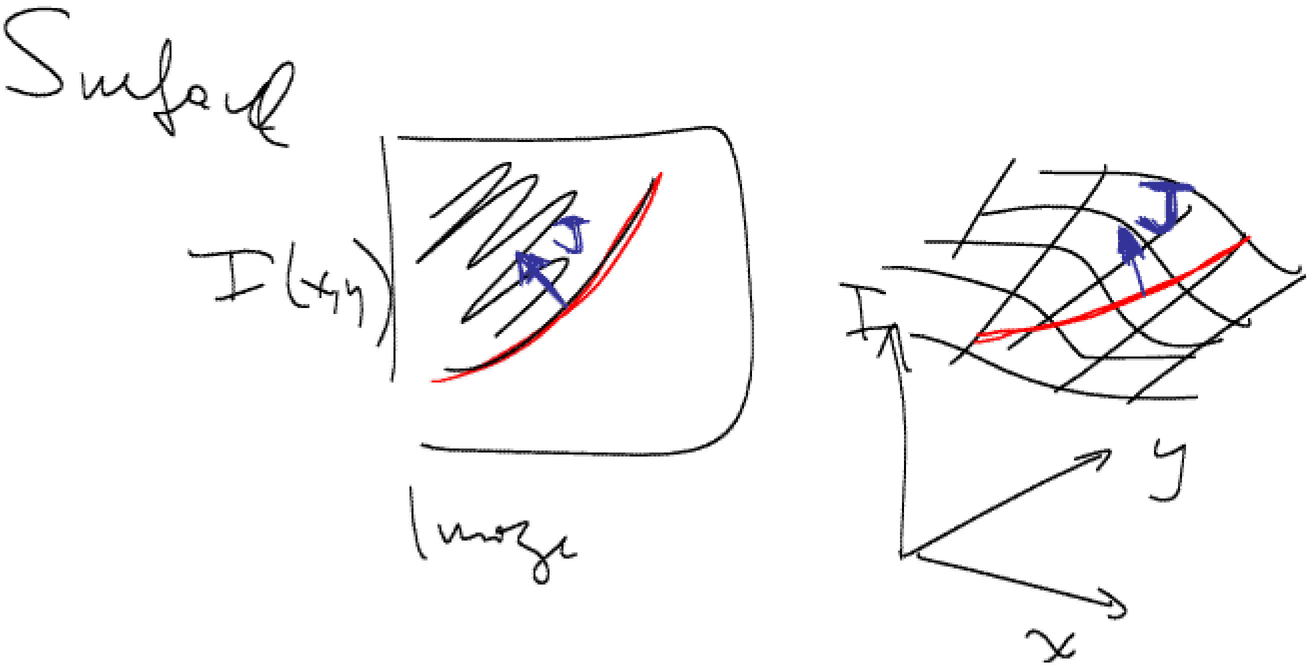

Figure 4.32: *Edge detection as slope finding in a height field. The local gradient vector points in the direction of greatest ascent and is perpendicular to the edge/contour orientation.*

The local gradient vector $\boldsymbol{J}$ points in the direction of *steepest ascent* in the intensity function. Its magnitude is an indication of the slope or strength of the variation, while its orientation points in a direction *perpendicular* to the local contour (Figure 4.32).

Unfortunately, taking image derivatives accentuates high frequencies and hence amplifies noise (since the proportion of noise to signal is larger at high frequencies). It is therefore necessary to smooth the image with a low-pass filter prior to computing the gradient. Because we would like the response of our edge detector to be independent of orientation, a circularly symmetric smoothing filter is desirable. As we saw in §3.2.1, the Gaussian is the only separable circularly-symmetric filter, and so it is used in most edge detection algorithms. Canny (1986) discusses alternative filters, and (Nalwa and Binford 1986, Nalwa 1987, Deriche 1987, Freeman and Adelson 1991, Nalwa 1993, Heath *et al.* 1998, Crane 1997, Ritter and Wilson 2000, Bowyer *et al.* 2001) review alternative edge detection algorithms and compare their performance.

Because differentiation is a linear operation, it commutes with other linear filtering operations. The gradient of the smoothed image can therefore be written as

$$\boldsymbol{J}_\sigma(\boldsymbol{x}) = \nabla[G_\sigma(\boldsymbol{x}) * I(\boldsymbol{x})] == [\nabla G_\sigma](\boldsymbol{x}) * I(\boldsymbol{x}), \tag{4.20}$$

i.e., we can convolve the image with the horizontal and vertical derivatives of the Gaussian kernel function,

$$\nabla G_\sigma(\boldsymbol{x}) = (\frac{\partial G_\sigma}{\partial x}, \frac{\partial G_\sigma}{\partial y})(\boldsymbol{x}) = [-x \;\; -y]\frac{1}{\sigma^3}\exp\left(-\frac{x^2+y^2}{2\sigma^2}\right) \tag{4.21}$$

(The parameter σ indicates the width of the Gaussian.) This is the same computation that is performed by Freeman and Adelson's (1991) first order steerable filter, which we already covered in §3.2.1 (3.27–3.28).

Figure 4.33b–c shows the result of convolving an image with the gradient of two different Gaussians. The direction of the gradient is encoded as the hue, and its strength is encoded as the saturation/value. As you can see, the gradients are stronger is areas corresponding to what we would perceive as edges.

For many applications, however, we wish to *thin* such a continuous image to only return isolated edges, i.e., as single pixels or *edgels* at discrete locations along the edge contours. This can be achieved by looking for *maxima* in the edge strength (gradient magnitude) in a direction *perpendicular* to the edge orientation, i.e., along the gradient direction. *[Note: It may be more convenient to just define the edge orientation as being the same as that of the (signed) gradient, i.e., pointing from dark to light. See Figure 2.2 for an illustration of the normal vector $\hat{\boldsymbol{n}}$ used to represent a line, and the local line equation becomes $(\boldsymbol{x} - \boldsymbol{x}_i) \cdot \hat{\boldsymbol{n}}_i = 0$. This will make subsequent Hough transform explanation simpler.]*

Finding this maximum corresponds to taking a directional derivative of the strength field in the direction of the gradient and then looking for zero crossings. The desired directional derivative is equivalent to the dot product between a second gradient operator and the results of the first,

$$S_\sigma(\boldsymbol{x}) = \nabla \cdot \boldsymbol{J}_\sigma(\boldsymbol{x}) = [\nabla^2 G_\sigma](\boldsymbol{x}) * I(\boldsymbol{x})]. \tag{4.22}$$

The gradient operator dot produced with the gradient is called the *Laplacian*. The convolution kernel

$$\nabla^2 G_\sigma(\boldsymbol{x}) = \frac{1}{\sigma^3}\left(2 - \frac{x^2+y^2}{2\sigma^2}\right)\exp\left(-\frac{x^2+y^2}{2\sigma^2}\right) \tag{4.23}$$

is therefore called the *Laplacian of Gaussian* (LoG) kernel (Marr and Hildreth 1980). This kernel can be split into two separable parts,

$$\nabla^2 G_\sigma(\boldsymbol{x}) = \frac{1}{\sigma^3}\left(1 - \frac{x^2}{2\sigma^2}\right)G_\sigma(x)G_\sigma(y) + \frac{1}{\sigma^3}\left(1 - \frac{y^2}{2\sigma^2}\right)G_\sigma(y)G_\sigma(x) \tag{4.24}$$

(J. S. Wiejak and Buxton 1985).

In practice, it is quite common to replace the Laplacian of Gaussian convolution with a Difference of Gaussian (DoG) computation, since the kernel shapes are qualitatively similar (Figure 3.37). This is especially convenient if a "Laplacian pyramid" §3.4 has already been computed.[4]

[4] Recall that Burt and Adelson's (1983a) "Laplacian pyramid" actually computed differences of Gaussian-filtered levels.

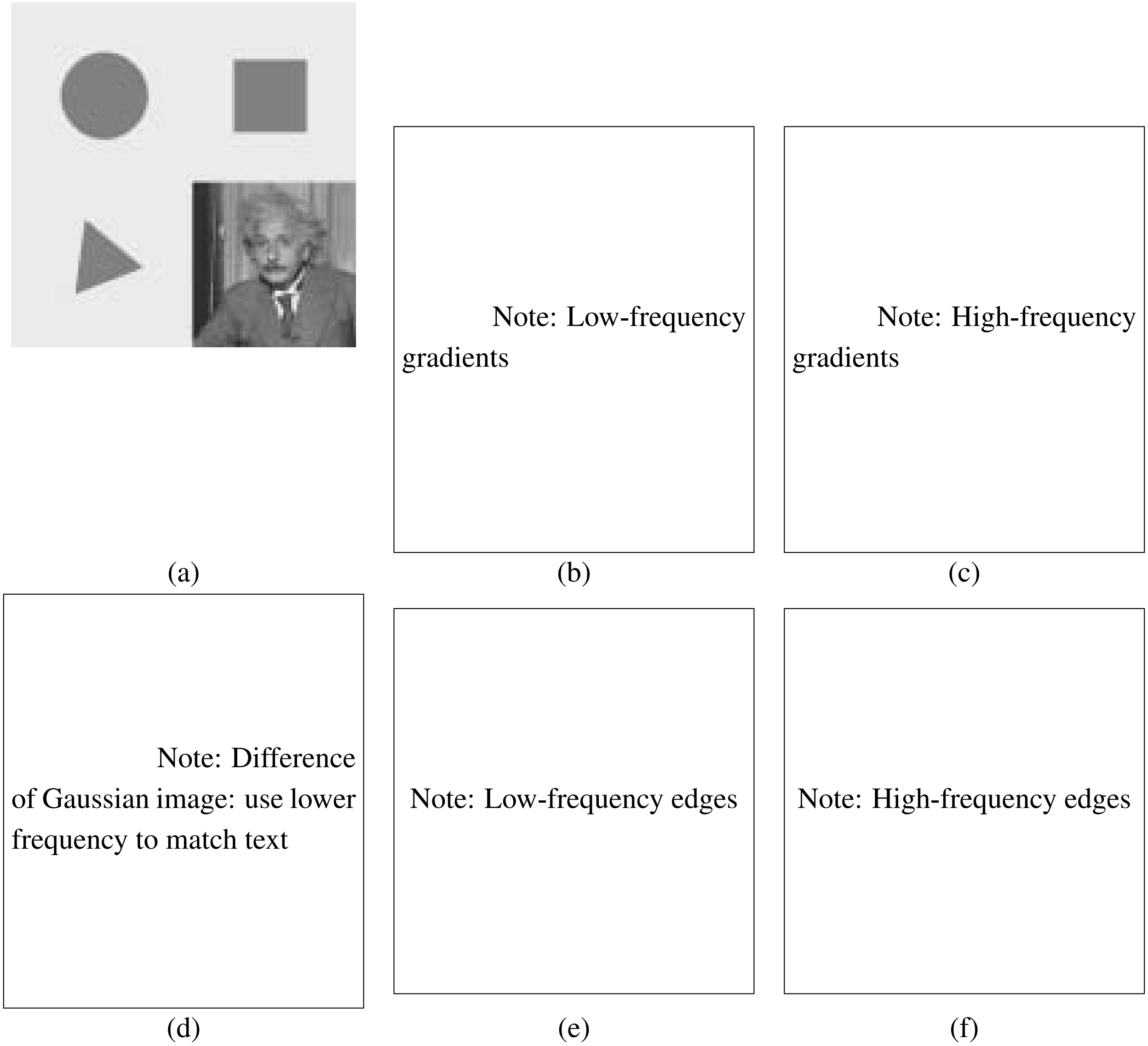

Note: Low-frequency gradients

Note: High-frequency gradients

(a) (b) (c)

Note: Difference of Gaussian image: use lower frequency to match text

Note: Low-frequency edges

Note: High-frequency edges

(d) (e) (f)

Figure 4.33: *Edge detection: (a) input image; (b) low-frequency gradients, color-coded for orientation and strength; (c) high-frequency gradients; (d) band-pass (Difference of Gaussian) filtered image; (e) low-frequency edges; (f) high-frequency edges. The detected edges are coded both by their strength (saturation) and orientation (hue).*

[Note: Generate these images. How do we detect edges? Multiply zero crossing by strength? May also want an additional row of results for just the gradient magnitude?]

Figure 4.33d shows the input image convolved with a Difference of Gaussian at the lower frequency. Taking the zero crossings of such an image (at the appropriate frequency) and multiplying it with the gradient magnitudes results in the edge images shown in Figure 4.33e–f.

In fact, it is not strictly necessary to take differences between adjacent levels when computing the edge field. *[Note: Watch out: if you take a larger area average, smaller bar-like edges will have their threshold shifted up/down. Better check if having a larger parent level actually helps.]* Think about what a zero crossing an a "generalized" difference of Gaussians image represents. The finer (smaller kernel) Gaussian is a noise-reduced version of the original image. The coarser (larger kernel) Gaussian is an estimate of the average intensity over a larger region. Thus, whenever the DoG image changes sign, this corresponds to the (slightly blurred) image going from relatively darker to relatively lighter, as compared to the average intensity in that neighborhood. *[Note: In fact, it may not be necessary to compute the gradient magnitude and direction first, but just to operate on the DoG image directly. Need to check what my current code does, and compare the results, or leave that to an exercise.]*

Once we have computed the signed function $S(\boldsymbol{x})$, we must find its *zero crossings* and convert these into edge elements or *edgels*. Figure 4.34a shows a pixel grid with some sample values of $S(\boldsymbol{x})$ at discrete locations indicated as black or white circles. An easy way to detect and represent zero crossings is to look for adjacent pixel locations $\boldsymbol{x}_i$ and $\boldsymbol{x}_j$ where the sign changes value, i.e., $[S(\boldsymbol{x}_i) > 0] \neq [S(\boldsymbol{x}_j) > 0]$.

The sub-pixel location of this crossing can be obtained by computing the "x-intercept" of the "line" connecting $S(\boldsymbol{x}_i)$ and $S(\boldsymbol{x}_j)$, as shown in Figure 4.34b,

$$\boldsymbol{x}_{\mathrm{z}} = \frac{\boldsymbol{x}_i S(\boldsymbol{x}_j) - \boldsymbol{x}_j S(\boldsymbol{x}_i)}{S(\boldsymbol{x}_j) - S(\boldsymbol{x}_i)}. \tag{4.25}$$

Figure 4.34a shows the detected edgels as small oriented red line segments living on a grid *dual* to the original pixel grid. The orientation and strength of such edgels can be obtained by linearly interpolating the gradient values computed on the original pixel grid.

An alternative edgel representation can be obtained by linking adjacent edgels on the dual grid to form edgels that live *inside* each square formed by four adjacent pixels in the original pixel grid, as shown by the blue line segments in Figure 4.34a.[5] The (potential) advantage of this representation is that the edgels now live on a grid offset by a $1/2$-pixel from the original pixel grid, and are thus easier to store and access. *[Note: This last sentence may not be that clear. Give more details in Exercise 4.8.]* As before, the orientations and strengths of the edges can be computed by interpolating the gradient field or estimating these values from the difference of Gaussian image (see Exercise 4.8). *[Note: Defer the discussion of the topology confusion to the linking section.]*

[5] This algorithm is a 2D version of the 3D *marching cubes* isosurface extraction algorithm (Lorensen and Cline 1987).

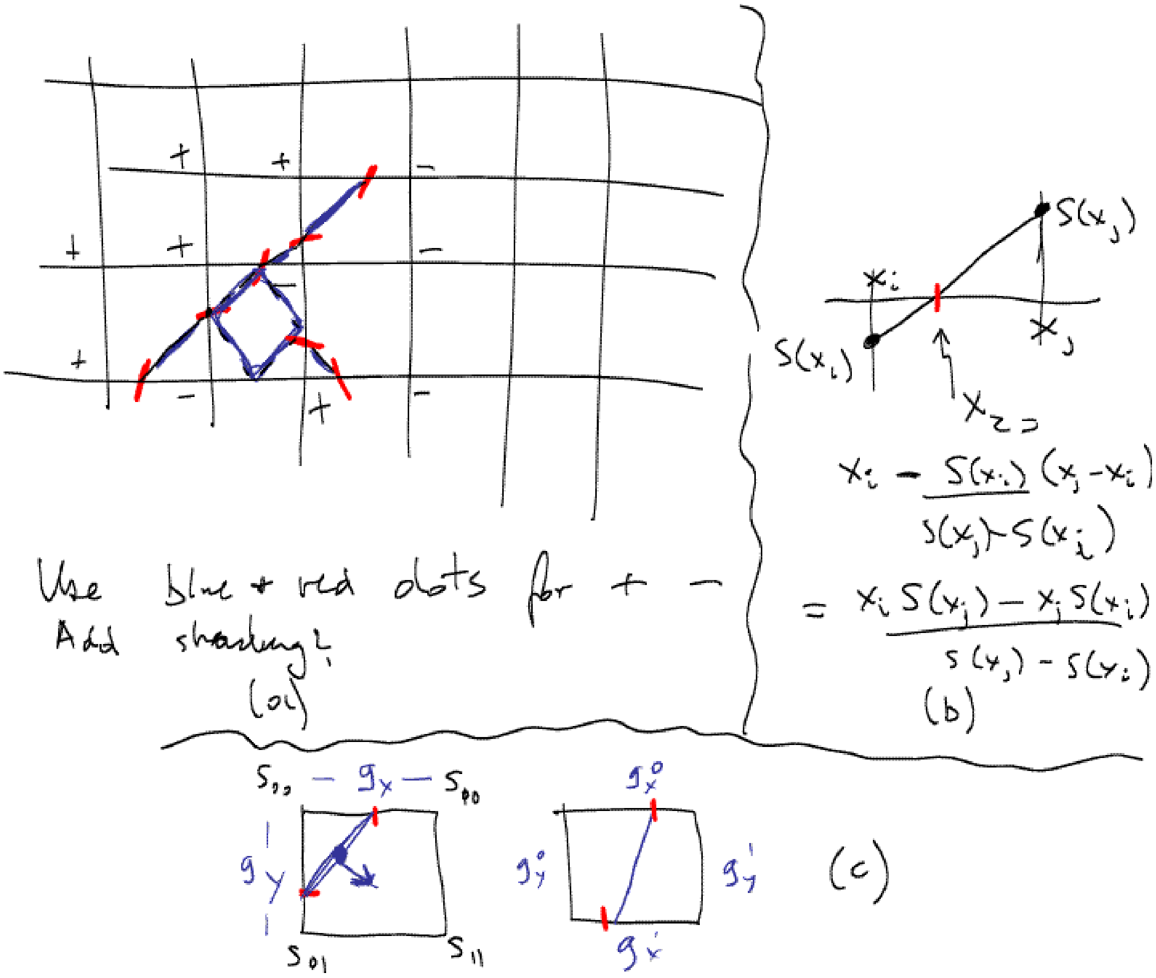
+ + −
+ + −
+ − + −
Use blue + red dots for + −
Add shading?
(a)
$S(x_j)$
x_i
$S(x_i)$
x_j
$x_z =$
$x_i - \frac{S(x_i)(x_j - x_i)}{S(x_j) - S(x_i)}$
$= \frac{x_i S(x_j) - x_j S(x_i)}{S(x_j) - S(x_i)}$
(b)
S_{00} — g_x — S_{10}
g_y
S_{01}
S_{11}
g_x^0
g_y^0
g_y^1
g_x^1
(c)

Figure 4.34: *Detecting and linking zero crossings in a Laplacian of Gaussian image. The signed values along horizontal and vertical edges can be used to locate the edgels to sub-pixel precision. The zero crossing topology may be ambiguous when the positive and negative values alternate around a square.*

[Note: Generate a proper figure]

In applications where the accuracy of the edge orientation is more important, higher-order steerable filters can be used (Freeman and Adelson 1991), §3.2.1. Such filters are more selective for more elongated edges, and also have the possibility of better modeling curve intersections because they can represent multiple orientations at the same pixel (Figure 3.15). Their disadvantage is that they are more computationally expensive to compute and the directional derivative of the edge strength does not have a simple closed form solution.[6] *[Note: I was going to say that you cannot as easily find the maximum, but my CVisSteerableFilter code seems to do that. It does it by computing a strength and orientation field at each pixel, then taking directional derivatives (using central differences) of the strength field (see* `find_maxima()`*). During the zero crossing computation, inconsistent angles are checked for and the derivative values are negated, as necessary. Need to re-read (Freeman and Adelson 1991) carefully and revive the code so that I can generate some figures here...]*

Scale selection and blur estimation

As we mentioned before, the derivative, Laplacian, and Difference of Gaussian filters (4.20–4.23) all require the selection of a spatial scale parameter σ. If we are only interested in detecting sharp edges, the width of the filter can be determined from image noise characteristics (Canny 1986, Elder and Zucker 1998). However, if we want to detect edges that occur at different resolutions (Figures 4.35b–c), a *scale-space* approach that detects and then selects edges at different scales may be necessary (Witkin 1983, Lindeberg 1994, Lindeberg 1998a, Nielsen *et al.* 1997).

Elder and Zucker (1998) present a principled approach to solving this problem. Given a known image noise level, their technique computes for every pixel the minimum scale at which an edge can be reliably detected (Figure 4.35d). Their approach first computes gradients densely over an image by selecting among gradient estimates computed at different scales (based on their gradient magnitudes). It then performs a similar estimate of minimum scale for directed second derivatives, and then uses zero crossings of this latter quantity to robustly select edges. (Figures 4.35e–f). As an optional final step, the blur width of each edge can be computed from the distance between extrema in the second derivative response minus the width of the Gaussian filter.

Color edge detection

While most edge detection techniques have been developed for grayscale images, color images can provide additional information. For example, noticeable edges between *iso-luminant* colors (colors that have the same luminance) are useful cues, but will fail to be detected by grayscale edge operators.

[6] In fact, the edge orientation can have a 180° ambiguity for "bar edges", which makes the computation of zero crossings in the derivative more tricky.

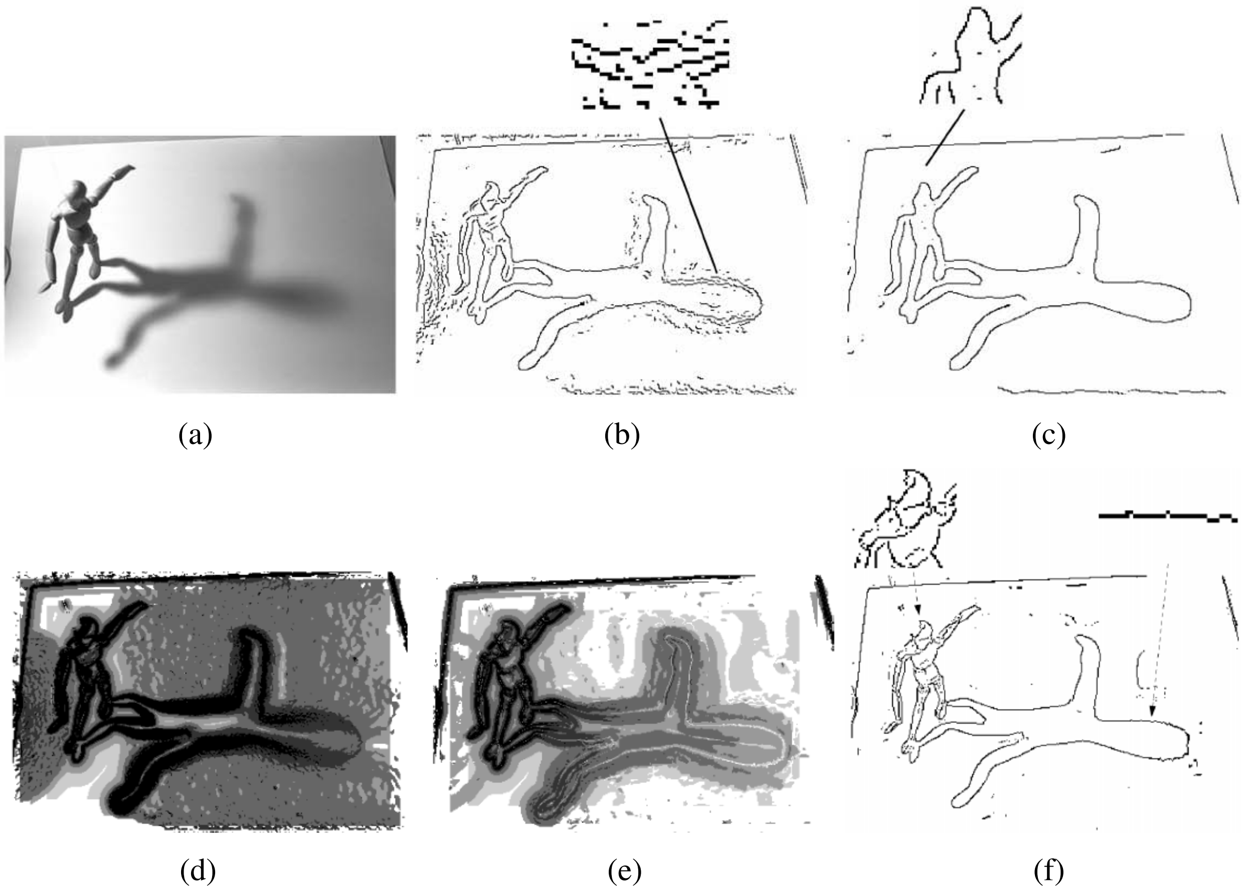

Figure 4.35: *Scale selection for edge detection (Elder and Zucker 1998). (a) original image; (b–c) Canny/Deriche edge detector tuned to the finer (mannequin) and coarser (shadow) scales; (d) minimum reliable scale for gradient estimation; (e) minimum reliable scale for second derivative estimation; (f) final detected edges.*

One simple approach is to combine the outputs of grayscale detectors run on each color band separately.[7] However, some care must be taken. For example, if we simply sum up the gradients in each of the color bands, the signed gradients may actually cancel each other! (Consider, for example a pure red-to-green edge.) We could also detect edges independently in each band and then take the union of these, but this might lead to thickened or doubled edges that are hard to link.

A better approach is to compute the *oriented energy* in each band (Morrone and Burr 1988, Perona and Malik 1990a), e.g., using a second order steerable filter §3.2.1 (Freeman and Adelson 1991), and to then sum up the orientation-weighted energies and find their joint best orientation.

[7] Instead of using the raw RGB space, a more perceptually uniform color space such as L*a*b* §2.3.2 can be used instead. When trying to match human performance (Martin *et al.* 2004), this makes sense. However, in terms of the physics of the underlying image formation and sensing, this may be questionable.

Unfortunately, the directional derivative of this energy may not have a closed form solution (as in the case of signed first order steerable filters), so a simple zero crossing-based strategy cannot be used. However, the technique described by Elder and Zucker (1998) can be used to numerically compute these zero crossings instead.

An alternative approach is to estimate local color statistics in regions around each pixel (Ruzon and Tomasi 2001, Martin *et al.* 2004). This has the advantage that more sophisticated techniques can be used to compare regional statistics (e.g., 3D color histograms) and that additional measures, such as texture, can also be considered. Figure 4.36 shows the output of such detectors.

Of course, many other approaches have been developed for detecting color edges, dating back to early work by Nevatia (1977). Ruzon and Tomasi (2001) and Gevers *et al.* (2006) provide good reviews of these approaches, which include ideas such as fusing outputs from multiple channels, using multidimensional gradients, and vector-based methods.

Combining edge feature cues

If the goal of edge detection is to match human *boundary detection* performance (Bowyer *et al.* 2001, Martin *et al.* 2004), as opposed to simply finding stable features for matching, even better detectors can be constructed by combining multiple low-level cues such as brightness, color, and texture.

Martin *et al.* (2004) describe a system that combines brightness, color, and texture edges to produce state-of-the-art performance on a database of hand-segmented natural color images (Martin *et al.* 2001). First, they construct and train separate oriented half-disc detectors for measuring significant differences in brightness (luminance), color (a* and b* channels, summed responses), and texture (un-normalized filter bank responses from (Malik *et al.* 2001)). (The training uses 200 labeled image, and testing is performed on a different set of 100 images.) Next, some of these responses are sharpened using a soft non-maximal suppression technique. Finally, the outputs of the three detectors are combined using a variety of machine learning techniques, among which, logistic regression is found to have the best speed-space-accuracy tradeoff. The resulting system (see Figure 4.36 for some visual examples) is shown to outperform previously developed techniques. In more recent work, Maire *et al.* (2008) improve on these results by combining the local appearance based detector with a *spectral* (segmentation-based) detector (Belongie and Malik 1998). *[Note: Even more recently,* Arbelaez et al. *(2009) build a hierarchical segmentation on top of this edge detector using a variant of the watershed algorithm.]*

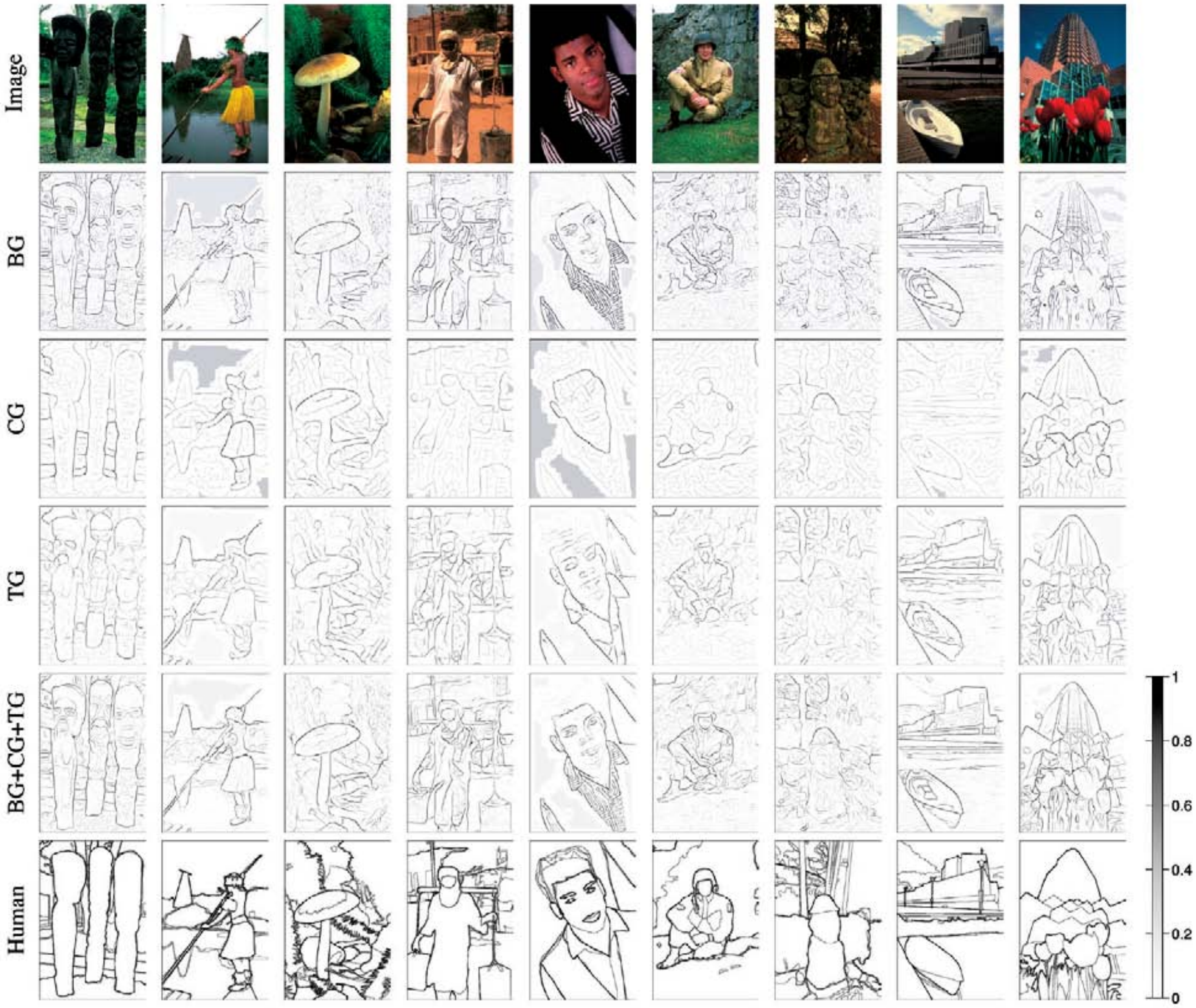

Figure 4.36: *Combined brightness/color/texture boundary detector (Martin* et al. *2004). Successive rows show the outputs of the brightness gradient (BG), color gradient (CG), texture gradient (TG), and combined (BG+CG+TG) detectors. The final row shows human-labeled boundaries derived from a database of hand-segmented images (Martin* et al. *2001).*

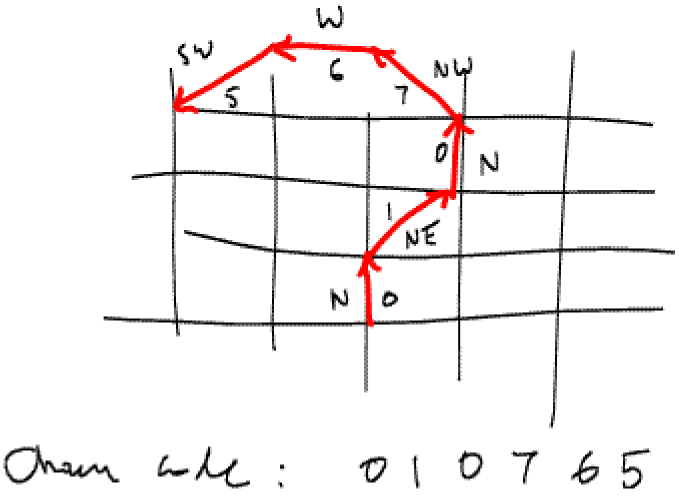

Figure 4.37: *Chain code representation of a grid-aligned linked edge chain. The code is represented as a series of direction codes, e.g, 0 1 0 7 6 5, which can further be compressed.*

4.2.2 Edge linking

While isolated edges can be useful for a variety of applications such as line detection §4.3 and sparse stereo matching §11.2, they become even more useful when linked into continuous contours.

If the edges have been detected using zero crossings of some function, linking them up is straightforward, since adjacent edgels share common endpoints (Figure 4.34a). Linking the edgels into chains involves picking up an unlinked edgel and following its neighbors in both directions. Either a sorted list of edgels (sorted first say by x coordinates and then y coordinates) or a 2D array can be used to accelerate the neighbor finding. If edges were not detected using zero crossings, finding the continuation of an edgel can be tricky. In this case, comparing the orientation (and optionally phase) of adjacent edgels can be used for disambiguation. Ideas from connected component computation can also sometimes be used to make the edge linking process even faster (see Exercise 4.9).

Once the edgels have been linked into chains, we can apply an optional thresholding with hysteresis to remove low-strength contour segments (Canny 1986). *[Note: Do I need to say more here? If so, re-read Canny and describe this better.]*

Linked edgel lists can be encoded more compactly using a variety of alternative representations. A *chain code* encodes a list of connected points lying on an $\mathcal{N}_8$ grid using a different 3-bit code corresponding to the eight cardinal directions (N, NE, E, SE, S, SW, W, NW) between a point and its successor (Figure 4.37). While this representation is more compact than the original edgel list (especially if predictive variable-length coding is used), it is not very suitable for further processing.

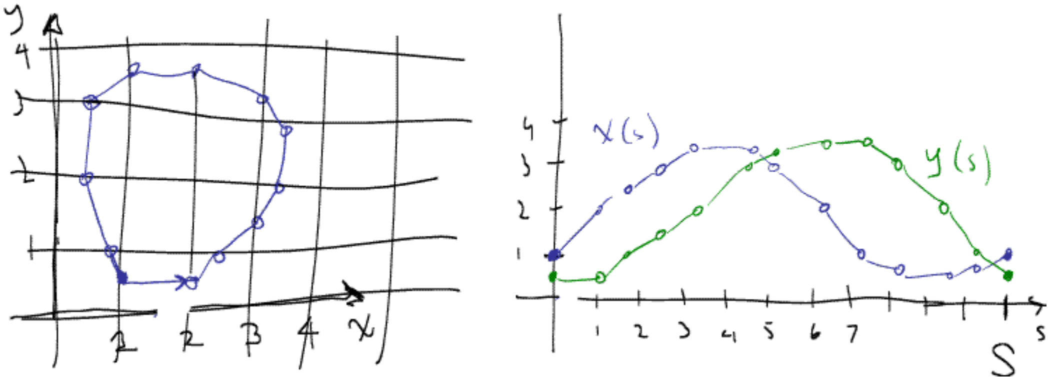

Figure 4.38: *Arc-length parameterization of a contour. Discrete points along the contour are first transcribed as (x, y) pairs along the arc length s. This curve can then be regularly re-sampled or converted into alternative (e.g., Fourier) representations.*

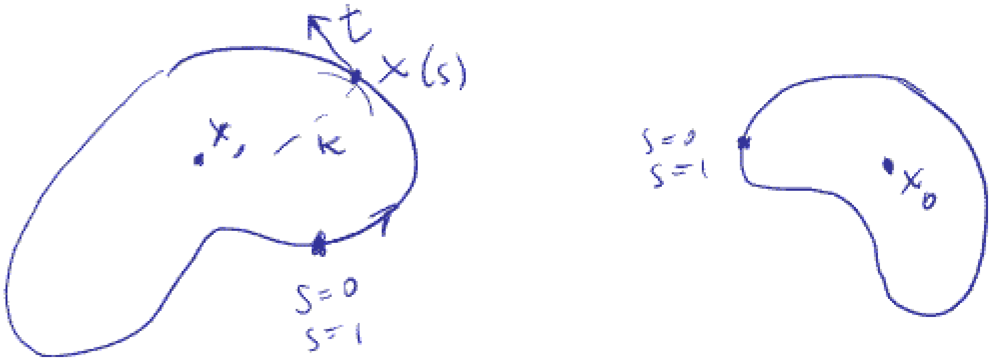

Figure 4.39: *Matching two contours using their arc-length parameterization. If both curves are normalized to unit length, $s \in [0, 1]$, they will have the same descriptor up to an overall "temporal" shift (due to different starting points for $s = 0$) and a phase (x-y) shift due to rotation.*

A more useful representation is the *arc-length parameterization* of a contour, $\boldsymbol{x}(s)$, where s denotes the arc length along a curve. Consider the linked set of edgels shown in Figure 4.38a. We start at one point (the solid dot at $(1.0, 0.5)$ in Figure 4.38a) and plot it at coordinate $s = 0$ (Figure 4.38b). The next point at $(2.0, 0.5)$ gets plotted at $s = 1$, and the next point at $(2.5, 1.0)$ gets plotted at $s = 1.7071$, i.e., we increment s by the length of each edge segment. The resulting plot can be resampled on a regular (say integral) s grid before further processing.

The advantage of the arc-length parameterization is that it makes matching and processing (e.g., smoothing) operations much easier. Consider the two curves describing similar shapes shown in Figure 4.39. To compare the curves, we first subtract the average values $\boldsymbol{x}_0 = \int_s \boldsymbol{x}(s)$ from each descriptor. Next, we rescale each descriptor so that s goes from 0 to 1 instead of 0 to S, i.e., we divide $\boldsymbol{x}(s)$ by S. Finally, we take the Fourier transform of each normalized descriptor,

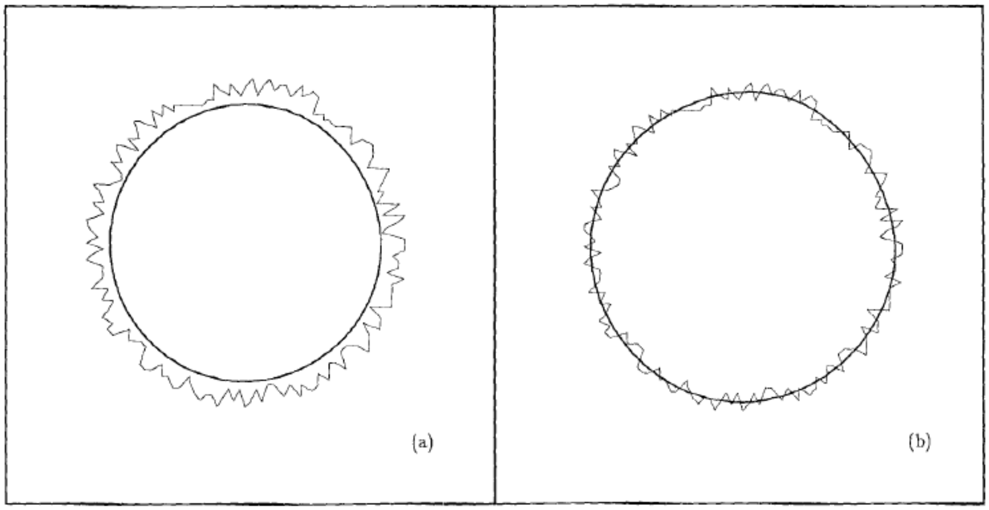

Figure 4.40: *Curve smoothing with a Gaussian kernel (Lowe 1988): (a) without shrinkage correction term; (b) with shrinkage correction term.*

treating each $\boldsymbol{x} = (x, y)$ value as a complex number. If the original curves are the same (up to an unknown scale and rotation), the resulting Fourier transforms should differ only by a scale change in magnitude plus a constant phase shift, due to rotation, and a linear phase shift, due to different starting points for s (see Exercise 4.10). *[Note: See if you can find a reference to this Fourier matching, either in a textbook or in some papers.]*

[Note: Read the papers below before finishing off this section:]

Lowe (1989): as we filter a 2D curve with a Gaussian, estimate the second derivatives of the smoothed curves (x and y separately), and then add back a term to compensate for the shrinkage (which is a function of radius and hence second derivative). See Figure 4.40. Taubin (1995) extends this technique by replacing the Lowe's offsetting step with one based on an additional (larger) smoothing...

An alternative approach, based on selectively modifying different frequencies in a wavelet decomposition, is presented by Finkelstein and Salesin (1994). In addition to controlling shrinkage without affecting its "sweep", wavelets allow the "character" of a curve to be interactively modified, as shown in Figure 4.41.

Kimia's curve evolution and skeleton-based descriptors: nice review article (Tek and Kimia 2003) and applications to recognition (Sebastian and Kimia 2005).

Also, shape contexts (Belongie *et al.* 2002).

Latest global contour grouping, completion, and junction detection (Maire *et al.* 2008): run normalized cuts (NC) on affinities derived from strongest Pb edge, then take gradients of eigenvectors to get "global Pb" and then later Pj (probability of junction) *[Note: Even more recently,*

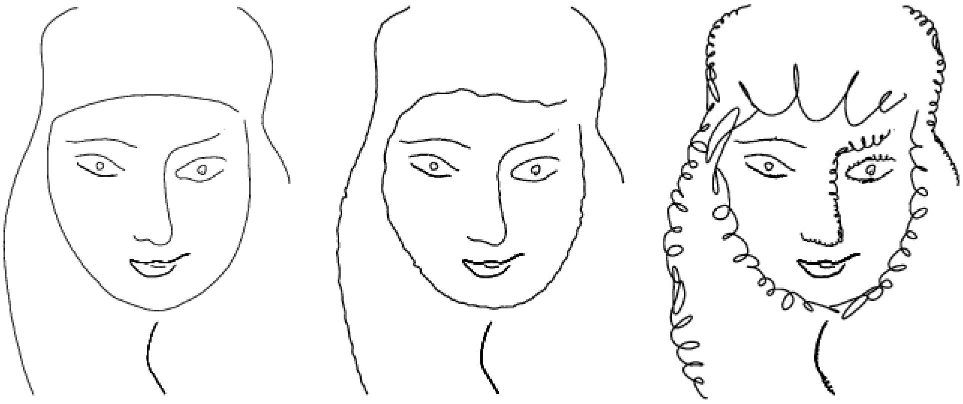

Figure 4.41: *Changing the character of a curve without affecting its sweep (Finkelstein and Salesin 1994): higher frequency wavelets can be replaced with exemplars from a style library to effect different local appearances.*

Arbelaez et al. *(2009) build a hierarchical segmentation on top of this edge detector using a variant of the watershed algorithm.]*

Point to (Maire *et al.* 2008) for other recent edge detectors and contour linkers.

Meltzer and Soatto (2008) have a nice edge descriptor based on scale-space analysis followed by gradient histograms on each side of the edge. Can be used for wide baseline stereo.

4.2.3 *Application*: Edge editing and enhancement

While edges can serve as components for object recognition or features for matching, they can also be used directly for image editing.

In fact, if the edge magnitude and blur estimate are kept along with each edge, a visually similar image can be reconstructed from this information (Elder 1999). Based on this principle, Elder and Golderg (2001) propose a system for "Image Editing in the Contour Domain". Their system allows users to selectively remove edges corresponding to unwanted features such as specularities, shadows, or distracting visual elements. After reconstructing the image from the remaining edges, the undesirable visual features have been removed (Figure 4.42).

Another potential application is to enhance perceptually salient edges while simplifying the underlying image to produce a cartoon-like or "pen-and-ink" like stylized image (DeCarlo and Santella 2002). This application is discussed in more detail in the section on non-photorealistic rendering §10.5.2.

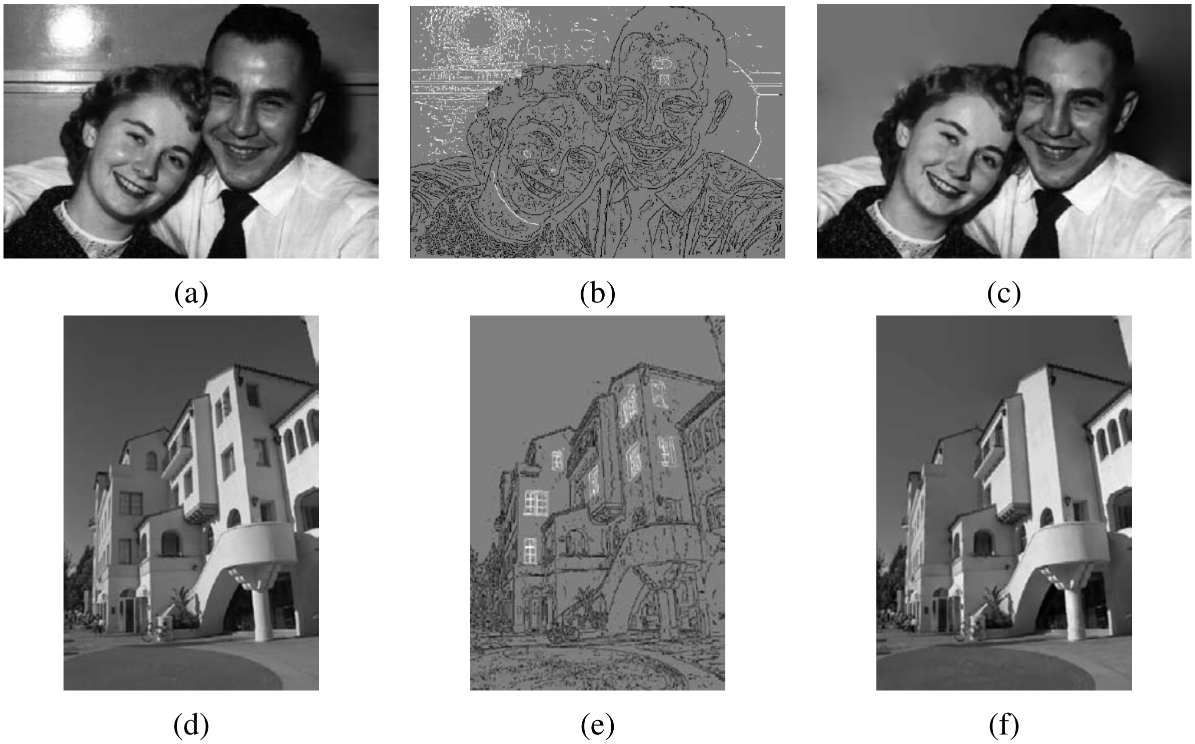

Figure 4.42: *Image editing in the contour domain (Elder and Golderg 2001). (a) & (d): original images; (b) & (e): extracted edges (edges to be deleted are marked in white); (c) & (f): reconstructed edited images.*

4.3 Lines

While edges and general curves are suitable for describing the contours of natural objects, the man-made worlds is full of straight lines. Detecting and matching these lines can be useful in a variety of applications, including architectural modeling, pose estimation in urban environments, and the analysis of printed document layouts.

[Note: Add a figure that shows each of the 3 cases (successive approx., Hough, VP) below?]

In this section, we present some techniques for extracting *piecewise linear* descriptions from the curves computed in the previous section. We begin with some algorithms for approximating a curve as a piecewise-linear polyline. We then describe the *Hough transform*, which can be used to group edgels into line segments even across gaps and occlusions. Finally, we describe how 3D lines with common *vanishing points* can be grouped together. These vanishing points can be used to calibrate a camera and to determine its orientation relative to a rectahedral scene, as described in §6.3.2.

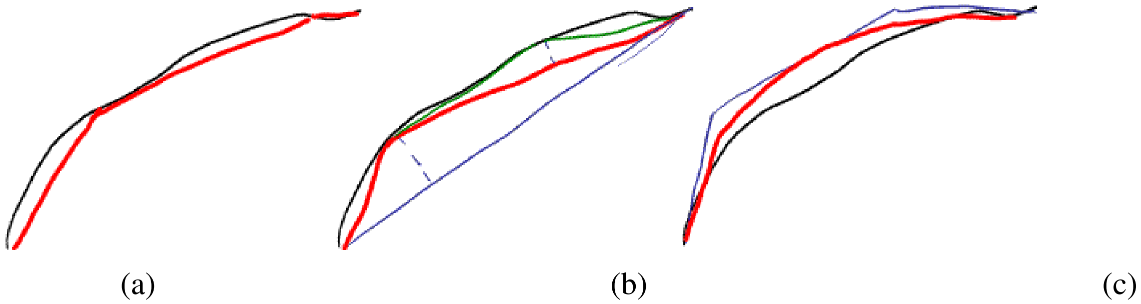

Figure 4.43: *Approximating a curve (shown in black) as a polyline or B-spline: (a) original curve and a polyline approximation shown in red; (b) successive approximation by recursively finding points furthest away from the current approximation (Ramer 1972, Douglas and Peucker 1973); (c) B-spline approximation, with the control net shown in blue and the B-spline shown in red.* *[Note: Visio does this when you draw a free-form curve: if you hover over the (smoothed) curve, you can see the Bezier control points.]*

4.3.1 Successive approximation

As we saw in the previous section 4.2.2, describing a curve as a series of 2D locations $\boldsymbol{x}_i = \boldsymbol{x}(s_i)$ provides a general representation suitable for matching and further processing. In many applications, however, it is preferable to approximate such a curve with a simpler representation, e.g., as a piecewise-linear polyline or as a B-spline curve (Farin 1996), as shown in Figure 4.43.

Many techniques have been developed over the years to perform this approximation, which is also known as *line simplification*. One of the oldest, and simplest, is the one simultaneously proposed by Ramer (1972) and Douglas and Peucker (1973), who recursively subdivide the curve at the point(s) the furthest away from the line(s) joining the two endpoints (or the current coarse polyline approximation), as shown in Figure 4.43. Hershberger and Snoeyink (1992) provide a more efficient implementation and also cite some of the other related work in this area.

Once the line simplification has been computed, it can be used to approximate the original curve. If a smoother representation or visualization is desired, either approximating or interpolating splines or curves can be used §3.4.1 and §5.1.1 (Szeliski and Ito 1986, Bartels *et al.* 1987, Farin 1996), as shown in Figure 4.43c.

4.3.2 Hough transforms

While curve approximation with polylines can often lead to successful line extraction, lines in the real world are sometimes broken up into disconnected components or made up of many collinear line segments (Figure 4.44). In many cases, it is desirable to group such collinear line segments into extended lines. As a further processing stage, described in the next section §4.3.3, we can then

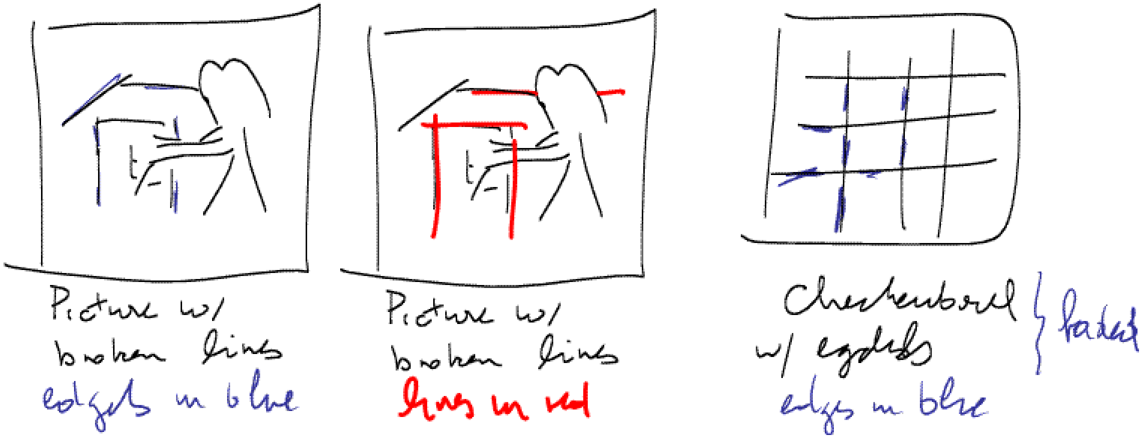

Figure 4.44: *Line fitting to discontinuous edge segments: (a) image with clutter; (b) fitted lines; (c) checkerboard image with missing edgels at corners.*

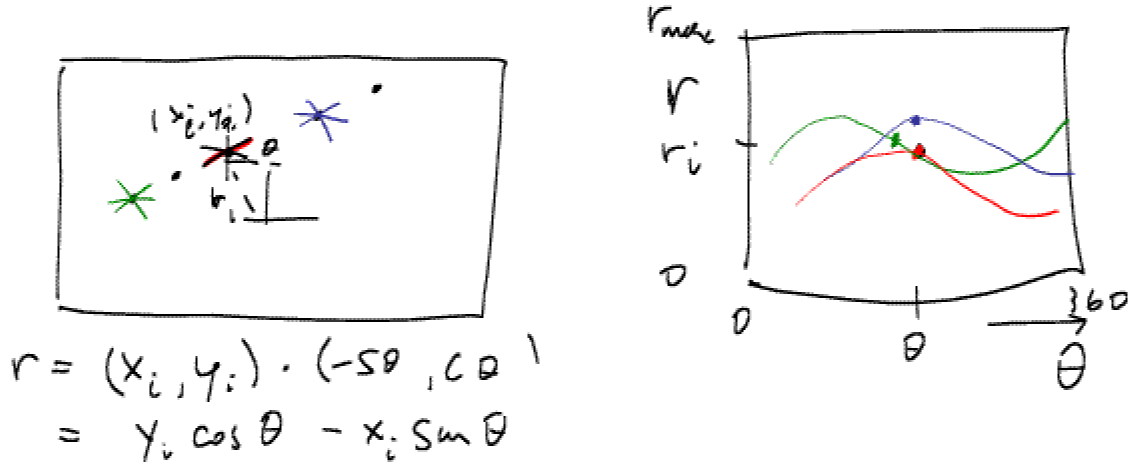

(a) (b)

Figure 4.45: *Original Hough transform: (a) each point votes for a complete family of potential lines* $r_i(\theta) = x_i \cos\theta + y_i \sin\theta$*; (b) each pencil of lines sweeps out a sinusoid in* (r, θ)*; their intersection provides the desired line equation.*

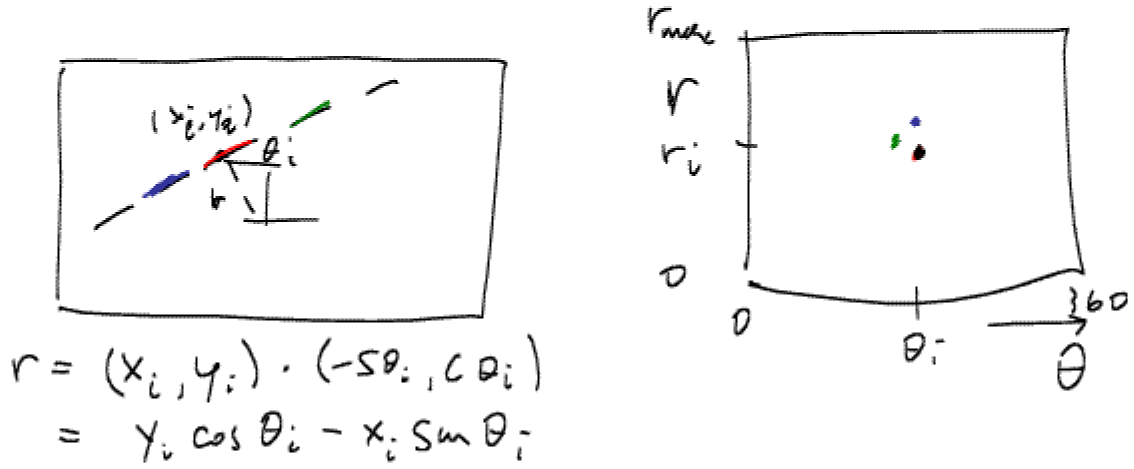
(x_i, y_i)
θ_i
r
$r = (x_i, y_i) \cdot (-s\theta_i, c\theta_i)$
$= y_i \cos\theta_i - x_i \sin\theta_i$
r_{max}
r
r_i
0
0
θ_i
360
θ

(a) (b)

Figure 4.46: *Hough transform: (a) an edgel re-parameterized in polar* (r, θ) *coordinates, with* $\hat{\boldsymbol{n}}_i = (\cos\theta_i, \sin\theta_i)$ *and* $r{=}\hat{\boldsymbol{n}}_i \cdot \boldsymbol{x}_i$*; (b)* (r, θ) *accumulator array, showing the votes for the three edgels marked in red, green, and blue.*

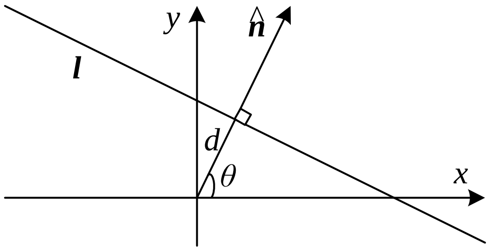

Figure 4.47: *2D line equation expressed in terms of the normal* $\hat{\boldsymbol{n}}$ *and distance to the origin* d *(coped from Figure 2.2).*

group such lines into collections with common vanishing points.

The Hough transform, named after its original inventor (Hough 1962), is a well-known technique for having edges "vote" for plausible line locations (Duda and Hart 1972, Ballard 1981, Illingworth and Kittler 1988) *[Note: Add more references: (Forsyth and Ponce 2003, Fitting Chapter); (Jähne 1997);]* In its original formulation (Figure 4.45), each edge point votes for *all* possible lines passing through it, and lines corresponding to high *accumulator* or *bin* values are examined for potential line fits.[8] Unless the points on a line are truly punctate, a better approach (in my experience) is to use the local orientation information at each edgel to vote for a *single* accumulator cell (Figure 4.46), as described below. A hybrid strategy, where each edgel

[8] The Hough transform can also be *generalized* to look for other geometric features such as circles (Ballard 1981), but we do not cover such extensions in this book.

votes for a number of possible orientation/location pairs centered around the estimate orientation, may be desirable in some cases.

Before we can vote for line hypotheses, we must first choose a suitable representation. Figure 4.47 (copied from Figure 2.2) shows the normal-distance $(\hat{\boldsymbol{n}}, d)$ parameterization for a line. Since lines are made up of edge segments, we adopt the convention that the line normal $\hat{\boldsymbol{n}}$ points in the same direction (has the same signs) as the image gradient $\boldsymbol{J}(\boldsymbol{x}) = \nabla I(\boldsymbol{x})$ (4.19). To obtain a minimal two-parameter representation for lines, we convert the normal vector into an angle

$$\theta = \tan^{-1} n_y / n_x, \tag{4.26}$$

as shown in Figure 4.47. The range of possible (θ, d) values is $[-180°, 180°] \times [-\sqrt{2}, \sqrt{2}]$, assuming that we are using normalized pixel coordinates (2.61) that lie in $[-1, 1]$. The number of bins to use along each axis depends on the accuracy of the position and orientation estimate available at each edgel and the expected line density, and is best set experimentally with some test runs on sample imagery.

Given the line parameterization, the Hough transform proceeds as follows: *[Note: turn into an algorithm]*

1. Clear the accumulator array.

2. For each detected edgel at location (x, y) and orientation $\theta = \tan^{-1} n_y / n_x$, compute the value of

   $$d = x\, n_x + y\, n_y \tag{4.27}$$

   and increment the accumulator corresponding to (θ, d).

3. Find the peaks in the accumulator corresponding to lines.

4. Optionally re-fit the lines to the constituent edgels.

Note that the original formulation of the Hough transform, which assumed no knowledge of the edgel orientation θ, has an additional loop inside of step 2 that iterates over all possible values of θ and increments a whole series of accumulators.

There are a lot of details in getting the Hough transform to work well, but these are best worked out by writing an implementation and testing it out on sample data. Exercise 4.14 describes some of these steps in more detail, including using edge segment lengths and/or strength during the voting process, keeping a list of constituent edgels in the accumulator array for easier post-processing, and optionally combining edges of different "polarity" into the same line segments.

An alternative to the 2D polar representation (θ, d) representation for lines is to use the full 3D $\boldsymbol{m} = (\hat{\boldsymbol{n}}, d)$ line equation, projected onto the unit sphere. While the sphere can be parameterized

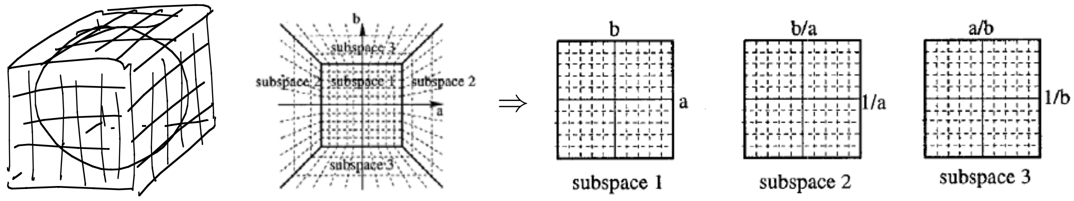

(a) (b)

Figure 4.48: *Cube map representation for line equations and vanishing points: (a) a cube map surrounding the unit sphere; (b) projecting the half-cube onto three sub-spaces (Tuytelaars* et al. *1997).*

using spherical coordinates (2.8),

$$\hat{\boldsymbol{m}} = (\cos\theta\cos\phi, \sin\theta\cos\phi, \sin\phi), \tag{4.28}$$

this does not uniformly sample the sphere and still requires the use of trigonometry.

An alternative representation can be obtained by using a *cube map*, i.e., projecting $\boldsymbol{m}$ onto the face of a unit cube (Figure 4.48a). To compute the cube map coordinate of a 3D vector $\boldsymbol{m}$, first find the largest (absolute value) component of $\boldsymbol{m}$, i.e., $m = \pm\max(|n_x|, |n_y|, |d|)$, and use this to select one of the six cube faces. Next, divide the remaining two coordinates by m and use these as indices into the cube face. While this avoids the use of trigonometry, it does require some decision logic.

One advantage of using the cube map, first pointed out by Tuytelaars *et al.* (1997) in their paper on the *Cascaded Hough Transform*, is that all of the lines passing through a point correspond to line segments on the cube faces, which is useful if the original (full voting) variant of the Hough transform is being used. In their work, they represent the line equation as $ax + b + y = 0$, which does not treat the x and y axes symmetrically. Note that if we restrict $d \geq 0$ by ignoring the polarity of the edge orientation (gradient sign), we can use a half-cube instead, which can be represented using only three cube faces (Figure 4.48b) (Tuytelaars *et al.* 1997).

Figure 4.49 shows the result of applying a Hough transform line detector to an image. As you can see, the technique successfully finds a lot of the extended lines in the image, but also occasionally find spurious lines due to the coincidental alignment of unrelated edgels. One way to reduce the number of spurious lines is to look for common vanishing points, as described in the next section §4.3.3.

RANSAC-base line detection. Another alternative to the Hough transform is the RANdom SAmple Consensus (RANSAC) algorithm described in more detail in §6.1.4. In brief, RANSAC randomly chooses pairs of edgels to form a line hypothesis and then tests how many other edgels fall onto this line. (If the edge orientations are accurate enough, a single edgel can produce this

Note: Some Hough-based line detection results

Figure 4.49: *Some Hough-based line detection results*
[Note: Show both accumulator array and overlaid lines]

hypothesis.) Lines with sufficiently large numbers of *inliers* (matching edgels) are then selected as the desired line segments.

An advantage of RANSAC is that no accumulator array is needed and so the algorithm can be more space efficient (and potentially less prone to the choice of bin size). The disadvantage is that many more hypotheses may be generated and tested than those obtained by finding peaks in the accumulator array.

In general, there is no clear consensus on which line estimation technique performs the best. It is therefore a good idea to think carefully about the problem at hand and to implement several approaches (successive approximation, Hough, and/or RANSAC) to determine the one that works best for your application.

4.3.3 Vanishing points

In many scenes, structurally important lines have the same vanishing point because they have they are parallel. Examples of such lines are horizontal and vertical building edges, zebra crossings, railway tracks, the edges of furniture such as tables and dressers, and of course, the ubiquitous calibration pattern (Figure 4.50). Finding the vanishing points common to such line sets can help refine their position in the image, and, in certain cases, help determine the intrinsic and extrinsic orientation of the camera §6.3.2.

Over the years, a large number of techniques have been developed for finding vanishing points, including (Quan and Mohr 1989, Collins and Weiss 1990, Brillaut-O'Mahoney 1991, McLean and Kotturi 1995, Becker and Bove 1995, Shufelt 1999, Tuytelaars *et al.* 1997, Schaffalitzky and Zisserman 2000, Antone and Teller 2000, Rother 2002, Košecká and Zhang 2005, Pflugfelder 2008)–see some of the more recent papers for additional references. In this section, we present

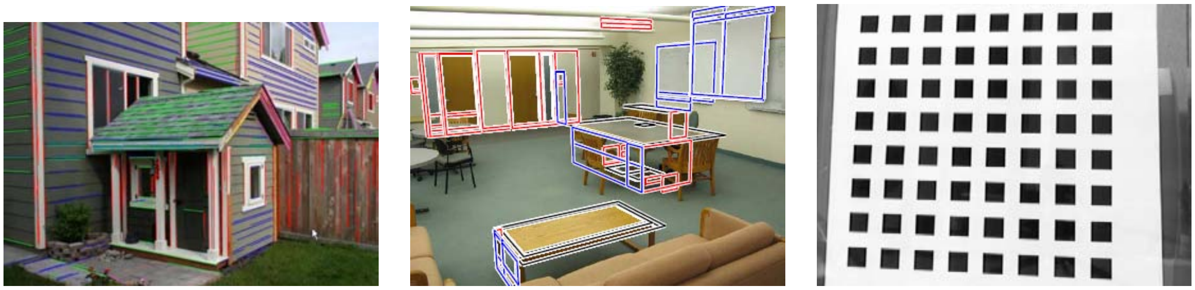

(a) (b) (c)

Figure 4.50: *Examples of real-world vanishing points: (a) architecture (Sinha* et al. *2008), (b) furniture (Mičušík* et al. *2008), and (c) calibration patterns (Zhang 1999).*

a simple Hough technique based on having line pairs vote for potential vanishing point locations, followed by a robust least squares fitting stage. For alternative approaches, please see some of the more recent papers listed above. *[Note: Re-read Roman Pflugfelder's thesis, (Pflugfelder 2008), which has a great literature review.]*

The first stage in my vanishing point detection algorithm uses a Hough transform to accumulate votes for likely vanishing point candidates. As with line fitting, one possible approach is to have each line vote for *all* possible vanishing point directions, either using a cube map (Tuytelaars *et al.* 1997, Antone and Teller 2000) or a Gaussian sphere (Collins and Weiss 1990), optionally using knowledge about the uncertainty in the vanishing point location to perform a weighted vote (Collins and Weiss 1990, Brillaut-O'Mahoney 1991, Shufelt 1999). My preferred approach is to use pairs of detected line segments to form candidate VP locations. Let $\hat{\boldsymbol{m}}_i$ and $\hat{\boldsymbol{m}}_j$ be the (unit norm) line equations for a pair of line segments and l_i and l_j be their corresponding segment lengths. The location of the corresponding vanishing point hypothesis can be computed as

$$\boldsymbol{v}_{ij} = \hat{\boldsymbol{m}}_i \times \hat{\boldsymbol{m}}_j \tag{4.29}$$

and the corresponding weight set to

$$w_{ij} = \|\boldsymbol{v}_{ij}\| l_i l_j. \tag{4.30}$$

This has the desirable effect of downweighting (near-)collinear line segments and short line segments. The Hough space itself can either be represented using spherical coordinates (4.28) or as a cube map (Figure 4.48a).

Once the Hough accumulator space has been populated, peaks can be detected in a manner similar to that previously discussed for line detection. Given a set of candidate line segments that voted for a vanishing point, which can optionally be kept as a list at each Hough accumulator cell, we then use a robust least squares fit to estimate a more accurate location for each vanishing point.

Consider the relationship between the two line segment endpoints $\{\boldsymbol{p}_{i0}, \boldsymbol{p}_{i1}\}$ and the vanishing point $\boldsymbol{v}$, as shown in Figure 4.51. The area A of the triangle given by these three points, which is

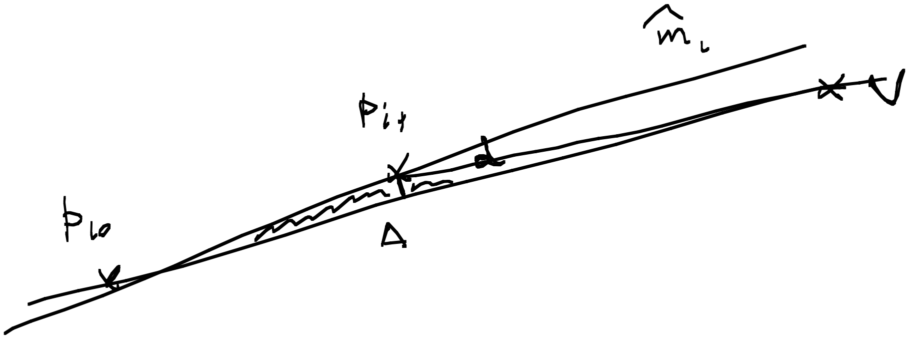

Figure 4.51: *Triple product of the line segments endpoints $\mathbf{p}_{i0}$ and $\mathbf{p}_{i1}$ and the vanishing point $\mathbf{v}$. The area A is proportional to the perpendicular distance d_1 and the distance between the other endpoint $\mathbf{p}_{i0}$ and the vanishing point.*

the magnitude of their triple product

$$A_i = |(\boldsymbol{p}_{i0} \times \boldsymbol{p}_{i1}) \cdot \boldsymbol{v}|, \tag{4.31}$$

is proportional to the perpendicular distance d_1 between each endpoint and the line through $\boldsymbol{v}$ and the other endpoint (as well as the distance between $\boldsymbol{p}_{i0}$ and $\boldsymbol{v}$). Assuming that the accuracy of a fitted line segment is proportional to the endpoint accuracy (Exercise 4.15), this therefore serves as a reasonable metric for how well a vanishing point fits a set of extracted lines. A robustified least squares estimate §B.3 for the vanishing point can therefore be written as

$$\mathcal{E} = \sum_i \rho(A_i) = \boldsymbol{v}^T \left(\sum_i w_i(A_i) \boldsymbol{m}_i \boldsymbol{m}_i^T \right) \boldsymbol{v} = \boldsymbol{v}^T \boldsymbol{M} \boldsymbol{v}, \tag{4.32}$$

where $\boldsymbol{m}_i = \boldsymbol{p}_{i0} \times \boldsymbol{p}_{i1}$ is the segment line equation weighted by its length l_i, and $w_i = \rho'(A_i)/A_i$ is the *influence* of each robustified (re-weighted) measurement on the final error §B.3. Notice how this metric is closely related to the original formula for the pairwise weighted Hough transform accumulation step. The final desired value for $\boldsymbol{v}$ is computed as the least eigenvector of $\boldsymbol{M}$.

While the technique described above proceeds in two discrete stages, better results may be obtained by alternating between assigning lines to vanishing points and refitting the vanishing point locations (Antone and Teller 2000, Košecká and Zhang 2005). The results of detecting individual vanishing points can also be made more robust by simultaneously searching for pairs or triplets of mutually orthogonal vanishing points (Shufelt 1999, Antone and Teller 2000, Rother 2002, Sinha *et al.* 2008). Some results of such vanishing point detection algorithms can be seen in Figure 4.50.

4.3.4 *Application*: Rectangle detection

Once sets of mutually orthogonal vanishing points have been detected, it now becomes possible to search for 3D rectangular structures in the image (Figure 4.52). Over the last decade, a vari-

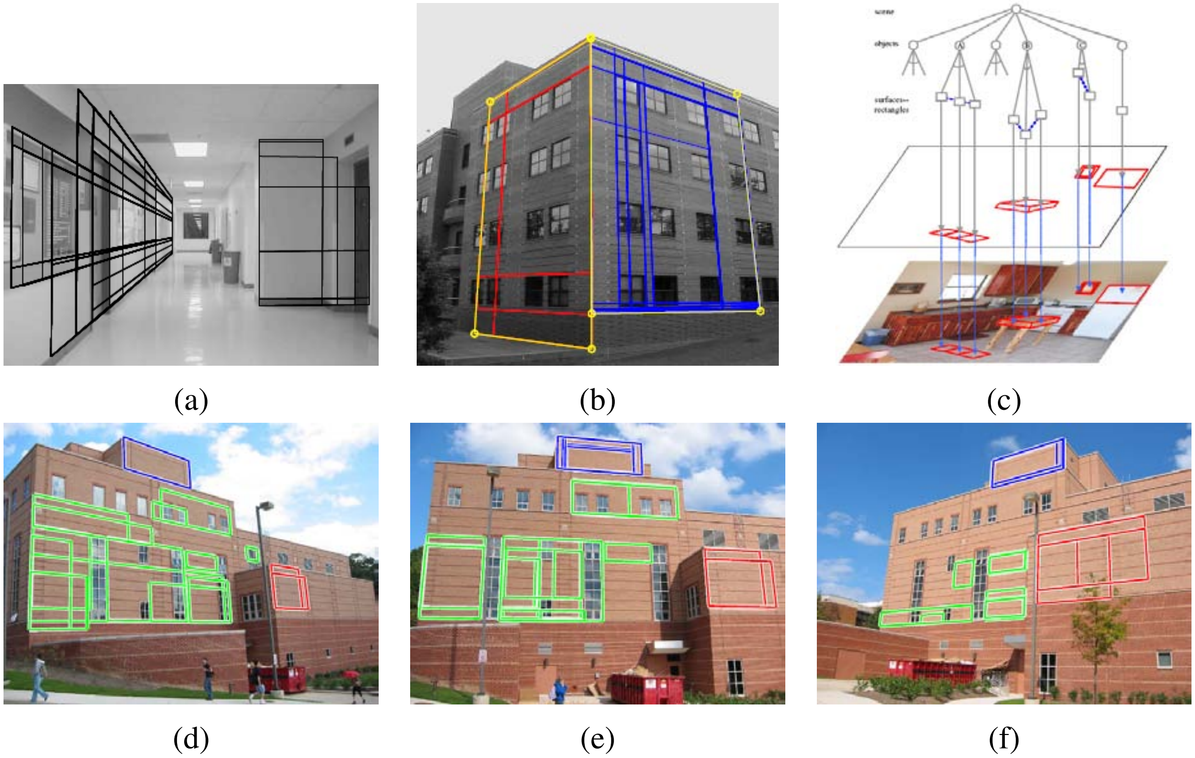

Figure 4.52: *Examples of rectangle detection: (a) indoor corridor and (b) building exterior with grouped facades (Košecká and Zhang 2005); (c) grammar-based recognition (Han and Zhu 2005); (d–e) rectangle matching using plane sweep (Mičušìk* et al. *2008).*

ety of techniques have been developed to find such rectangles, primarily focused on architectural scenes (Košecká and Zhang 2005, Han and Zhu 2005, Shaw and Barnes 2006, Mičušìk *et al.* 2008, Schindler *et al.* 2008).

After detecting orthogonal vanishing directions, Košecká and Zhang (2005) refine the fitted line equations, search for corners near line intersections, and then verify rectangle hypotheses by rectifying the corresponding patches and looking for a preponderance of horizontal and vertical edges (Figures 4.52a–b). In follow-on work, Mičušìk *et al.* (2008) use a Markov Random Field (MRF) to disambiguate between potentially overlapping rectangle hypotheses. They also use a plane sweep algorithm to match rectangles between different views (Figures 4.52d–f).

A different approach is proposed by Han and Zhu (2005), who use a grammar of potential rectangle shapes and nesting structures (between rectangles and vanishing points) to infer the most likely assignment of line segments to rectangles (Figure 4.52c).

4.4 Additional reading

[Note: Move some references here]

An early well-regarded paper on straight line extraction in images is (Burns *et al.* 1986).

4.5 Exercises

Ex 4.1 (Interest point detector) Implement one or more keypoint detectors and compare their performance (with your own, or with a classmate's)

Possible detectors:

1. Laplacian or Difference of Gaussian
2. Förstner-Harris Hessian (try different formula variants given in (4.9–4.11)).
3. oriented/steerable filter, either looking for 2nd order high 2nd response, or two edges in a window (Koethe 2003), discussed in §4.1.1.
4. others from (Mikolajczyk *et al.* 2005, Tuytelaars and Mikolajczyk 2007)

Additional optional steps could include:

1. Compute the detections on a sub-octave pyramid and find 3D maxima.
2. Find local orientation estimates (using steerable filter responses or a gradient histogramming method).
3. Implement non-maximal suppression, such as the adaptive technique of Brown *et al.* (2005).
4. Vary the window shape and size (pre-filter and aggregation).

To test for repeatability, download the code from `http://www.robots.ox.ac.uk/~vgg/software/` (Mikolajczyk *et al.* 2005, Tuytelaars and Mikolajczyk 2007), or simply rotate/shear your own test images (pick a domain you may want to use later, e.g., for outdoor stitching).

Measure the stability of your scale and orientation estimates as well.

Ex 4.2 (Interest point descriptor) Implement one or more descriptors (steered to local scale and orientation) and compare their performance (with your own, or with a classmate's)

Some possible descriptors include

1. contrast-normalized patches (Brown *et al.* 2005)

2. SIFT (Lowe 2004),

3. GLOH (Mikolajczyk and Schmid 2005),

4. DAISY (Winder and Brown 2007),

5. others from (Mikolajczyk and Schmid 2005)

(Figures 4.19–4.20). Optionally do this on a sub-octave pyramid, find 3D maxima.

Vary the choose window shape and size (pre-filter and aggregation);

Ex 4.3 (Feature matcher) *[Note: The following ideas are pretty old; update them:]*

Use SSD or correlation score; estimate bias/gain; use local feature vector (Schmid, Jets [Von Der Malsburg ?])

How about David Lowe's adaptive threshold idea, used in MOPS (Brown *et al.* 2005)?

See also §8.1.2 and Exercise 8.1 for more techniques and a more quantitative comparison.

Ex 4.4 (ROC curve computation) Given a pair of curves (histograms) plotting the number of matching and non-matching features as a function of Euclidean distance d as shown in Figure 4.23b, derive an algorithm for plotting an ROC curve (Figure 4.23a). In particular, let $t(d)$ be the distribution of true matches and $f(d)$ be the distribution of (false) non-matches. Write down the equations for the ROC, i.e., TPR(FPR), and the AUC.

Hint: Plot the cumulative distributions $T(d) = \int t(d)$ and $F(d) = \int f(d)$ and see if these help you derive the TPR and FPR at a given threshold θ.

Ex 4.5 (Image matcher—part 1) Select some set of image features (corners, lines, regions) that you can somewhat reliably match across images taken from disparate points of view. (Lowe 1999, Schaffalitzky and Zisserman 2002, Sivic and Zisserman 2003)

Later exercise will show how to combine this with camera motion / 3D structure to completely match the images.

Ex 4.6 (Feature tracker) find corresponding points, string together; (optional: winnow out matches with epipolar geometry or 3D – need material in next 2 chapters) add new points at each frame; evaluate quality of matches, terminate if necessary.

Note that affine registration used in (Shi and Tomasi 1994) is not introduced until §8.2 and Exercise 8.2.

Ex 4.7 (Facial feature tracker) initialize tracker on person's facial features, use it to drive a simple 2D morph of another face or cartoon (reuse morphing code from exercise in previous chapter)

```
struct SEdgel {
    float e[2][2];      // edgel endpoints (zero crossing)
    float x, y;         // sub-pixel edge position (midpoint)
    float n_x, n_y;     // orientation, as normal vector
    float theta;        // orientation, as angle (degrees)
    float length;       // length of edgel
    float strength;     // strength of edgel (local gradient magnitude)
};

struct SLine : public SEdgel {
    float line_length;  // length of line (estimated from ellipsoid)
    float sigma;        // estimated std. dev. of edgel noise
    float r;            // line equation: x * n_y - y * n_x = r
};
```

Table 4.2: *A potential C++ structure for edgel and line elements*

[Note: Use a smaller font for the code. Should these kinds of code snippets be moved into Appendix C.2?]

Ex 4.8 (Edge detector) Implement an edge detector of your choice. Compare its performance to that of other classmates', or from code downloaded from the Net.

A simple but well-performing sub-pixel edge detector can be created as follows:

1. Blur the input image a little,
$$B_\sigma(\boldsymbol{x}) = G_\sigma(\boldsymbol{x}) * I(\boldsymbol{x}).$$

2. Construct a Gaussian pyramid (Exercise refex:pyramid),
$$P = \text{Pyramid}\{B_\sigma(\boldsymbol{x})\}$$

3. Subtract an interpolated coarser-level pyramid image from the original resolution blurred image,
$$S(\boldsymbol{x}) = B_\sigma(\boldsymbol{x}) - P.\text{InterpolatedLevel}(L).$$

4. For each quad of pixels, $\{(i,j),(i+1,j),(i,j+1),(i+1,j+1)\}$, count the number of zero crossings along the four edges.

5. When there are exactly two zero crossing, compute their locations using (4.25) and store these edgel endpoints along with the midpoint in the edgel structure (Table 4.2).

6. For each edgel, compute the local gradient by taking the horizontal and vertical differences between the values of S along the zero crossing edges (Figure 4.34c). *[Note: Perhaps make this a separate figure closer to the end of this chapter.]*

7. Store the magnitude of this gradient as the edge strength, and either its orientation, or that of the segment joining the edgel endpoints, as the edge orientation.

8. Add the edgel to a list of edgels, or alternatively, store it in a 2D array of edgels (addressed by pixel coordinates).

Table 4.2 shows a possible representation for each computed edgel.

Ex 4.9 (Edge linking and thresholding) Link up the edges computed in the previous exercise into chains, and optionally perform thresholding with hysteresis.

Some suggested steps include:

1. Store the edgels either in a 2D array (say an integer image with indices into the edgel list), or pre-sort the edgel list first by (integer) x coordinates and then y coordinates, for faster neighbor finding.

2. Pick up an edgel from the the list of unlinked edgels, and find its neighbors in both directions until no neighbor is found, or a closed contour is obtained. Flag edgels as linked as you visit them, and push them onto your list of linked edgels.

3. Alternatively, generalize a previously developed connected component algorithm (Exercise 3.14) to perform the linking in just two raster passes.

4. [Optional] Perform hysteresis-based thresholding (Canny 1986). Starting at one end of the contour, walk along the contour until... *[Note: Re-read Canny to see if a good description exists there...]*

5. [Optional] Link together contours that have small gaps but whose endpoints have similar orientations.

6. [Optional] Find junctions between adjacent contours, e.g., using some of the ideas (or references) from (Maire *et al.* 2008).

Ex 4.10 (Contour matching) Convert a closed contour (linked edgel list) into its arc-length parameterization, and use this to match object outlines. *[Note: See some of Kimia's papers (Tek and Kimia 2003, Sebastian and Kimia 2005) for examples and references.]*

Some suggested steps include:

1. Walk along the contour and create a list of (x_i, y_i, s_i) triplets, using the arc-length formula

$$s_{i+1} = s_i + \|\boldsymbol{x}_{i+1} - \boldsymbol{x}_i\|. \tag{4.33}$$

2. Resample this list onto a regular set of (x_j, y_j, j) samples using linear interpolation of each segment.

3. Compute the average value of x and y, e.g., $\overline{x} = \sum_{j=0\ldots S} x_j$. (Careful: the value of $S = \max s_i$ is generally non-integral, so adjust your formula accordingly.)

4. [Variant] Directly resample the original (x_i, y_i, s_i) piecewise linear function onto a length-independent set of samples, say $j \in [0, 1023]$. (Using a power of 2 length will make subsequent Fourier transforms more convenient.)

5. Compute the Fourier transform of the curve, treating each (x, y) pair as a complex number.

6. To compare two curves, fit a linear equation to the phase difference between the two curves. (Careful: phase wraps around at $360°$. Also, you may wish to weight samples by their Fourier spectrum magnitude. See §8.1.2.)

7. [Optional] Prove that the constant phase component corresponds to the temporal shift in s, while the linear component corresponds to rotation.

Of course, feel free to try any other curve descriptor and matching technique from the computer vision literature.

Ex 4.11 (Jigsaw puzzle solver–project) Write a program to automatically solve a jigsaw puzzle from a set of scanned puzzle pieces. The project may include the following components:

1. Scan the pieces (either face up or face down) on a flatbed scanner with a distinctively colored background.

2. Optionally scan in the box top to use as a low-resolution reference image.

3. Use color-based thresholding to isolate the pieces.

4. Extract the contour of each piece using edge finding and linking.

5. Optionally re-represent each contour using an arc-length or some other re-parameterization. Break up the contours into meaningful matchable pieces (hard?).

6. Optionally associate color values with each contour to help in the matching.

7. Optionally match pieces to the reference image using some rotationally invariant feature descriptors.

8. Solve a global optimization or (backtracking) search problem to snap pieces together and/or place them in the correct location relative to the reference image.

9. Test your algorithm on a succession of more difficult puzzles, and compare your results with others'.

Ex 4.12 (Artistic rendering) application: ink-and-watercolor rendering (see above)...? *[Note: move this to Computational Photography chapters since we have an NPR section* §*10.5.2 there.]*

Ex 4.13 (Successive approximation line detector) Implement a line simplification algorithm §4.3.1 (Ramer 1972, Douglas and Peucker 1973) to convert a hand-drawn curve (or linked edge image) into a small set of polylines. Optionally, re-render this curve using either an approximating or interpolating spline or Bezier curve (Szeliski and Ito 1986, Bartels *et al.* 1987, Farin 1996).

Ex 4.14 (Hough transform line detector) Implement a Hough transform for finding lines in images:

1. Create an accumulator array of the appropriate use-specified size and clear it. The user can specify the spacing in degrees between orientation bins and in pixels between distance bins. The array can either be allocated as integer (for simple counts), floating point (for weighted counts), or as an array of vectors for keeping back pointers to the constituent edges.

2. For each detected edgel at location (x, y) and orientation $\theta = \tan^{-1} n_y/n_x$, compute the value of

$$d = xn_x + yn_y \tag{4.34}$$

and increment the accumulator corresponding to (θ, d). Optionally weight the vote of each edge by its length (see Exercise 4.8) and/or the strength of its gradient.

3. Optionally smooth the scalar accumulator array by adding in values from its immediate neighbors (this helps counteract the *discretization* effect of voting for only a single bin—see Exercise 3.7.

4. Find the largest peaks (local maxima) in the accumulator corresponding to lines.

5. For each peak, optionally re-fit the lines to the constituent edgels, using *total least squares* §A.2. In this step, optionally use the original edgel lengths and/or strength weights to weight the least squares fit, as well as potentially the agreement between the hypothesized line

orientation and the edgel orientation. Determine whether these heuristics help increase the accuracy of the fit.

6. After fitting each peak, zero-out or eliminate that peak and its adjacent bins in the array, and move on to the next largest peak.

Test out your Hough transform on a variety of images taken indoors and outdoors, as well as checkerboard calibration patterns.

For the latter case (checkerboard patterns), you can modify your Hough transform by collapsing *antipodal* bins $(\theta \pm 180°, -d)$ with (θ, d) to find lines that do not care about polarity changes. Can you think of examples in real world images where this might be desirable as well?

Ex 4.15 (Line fitting uncertainty) Estimate the uncertainty (covariance) in your line fit using uncertainty analysis.

1. After determining which edgels belong to the line segment (using either successive approximation or Hough transform), re-fit the line segment using total least square (Van Huffel and Vandewalle 1991, Huffel and Lemmerling 2002), i.e., find the mean/centroid of the edgels and then use eigenvalue analysis to find the dominant orientation.

2. Compute the perpendicular errors (deviations) to the line and robustly estimate the variance of the fitting noise using an estimator such as MAD §B.3.

3. Optionally re-fit the line parameters by throwing away outliers or using a robust norm / influence function.

4. Estimate the error in the perpendicular location of the line segment and its orientation

[Note: Need to work this out in more detail, and perhaps include the error analysis in the main text.]

Ex 4.16 (Vanishing points) Compute vanishing points and refine line equations. The results will used later to track a target (Exercise 6.5) or reconstruct architecture (Exercise ???)

Ex 4.17 (Vanishing point uncertainty) Perform an uncertainty analysis on your estimated vanishing points. You will need to decide how to represent your vanishing point, e.g., homogeneous coordinates on a sphere, to handle VPs near infinity.

See the discussion of Bingham distributions in (Collins and Weiss 1990).